Geologica Acta, Vol.14, Nº 3, September 2016, 237-259
DOI: 10.1344/GeologicaActa2016.14.3.3

geologica acta

Late Neoproterozoic layered mafic intrusion of arc-affinity in the Arabian-Nubian Shield: A case study from the Shahira layered mafic intrusion, southern Sinai, Egypt

M.K. AZER[1] M.A. OBEID[2] H.A. GAHLAN[3,4]

[1]Geological Sciences Department, National Research Centre
P.O.Box 12622-Dokki, Cairo, Egypt

[2]Geology Department, Faculty of Science, Fayoum University
P.O.Box 63514- Fayoum, Egypt

[3]Department of Geology and Geophysics College of Sciences, King Saud University
Riyadh 11451, Saudi Arabia

[4]Geology Department, Faculty of Science, Assiut University
Assiut, Egypt

ABSTRACT

The Shahira Layered Mafic Intrusion (SLMI), which belongs to the late Neoproterozoic plutonic rocks of the Arabian-Nubian Shield, is the largest layered mafic intrusion in southern Sinai. Field relations indicate that it is younger than the surrounding metamorphic rocks and older than the post-orogenic granites. Based on variation in mineral paragenesis and chemical composition, the SLMI is distinguished into pyroxene-hornblende gabbro, hornblende gabbro and diorite lithologies. The outer zone of the mafic intrusion is characterized by fine-grained rocks (chilled margin gabbroic facies), with typical subophitic and/or microgranular textures. Different rock units from the mafic intrusion show gradational boundaries in between. They show some indications of low grade metamorphism, where primary minerals are transformed into secondary ones. Geochemically, the Shahira layered mafic intrusion is characterized by enrichment in LILE relative to HFSE (*e.g.* Nb, P, Zr, Ti, Y), and LREE relative to HREE [(La/Lu)n= 4.75–8.58], with subalkaline characters. It has geochemical characteristics of pre-collisional arc-type environment. The geochemical signature of the investigated gabbros indicates partial melting of mantle wedge in a volcanic-arc setting, being followed by fractional crystallization and crustal contamination. Fractional crystallization processes played a vital role during emplacement of the Shahira intrusion and evolution of its mafic and intermediate rock units. The initial magma was evolved through crystallization of hornblende which was caused by slight increasing of H_2O in the magma after crystallization of liquidus olivine, pyroxene and Ca-rich plagioclase. The gabbroic rocks crystallized at pressures between 4.5 and 6.9kbar (~15–20km depth). Whereas, the diorites yielded the lowest crystallization pressure between 1.0 to 4.4Kbar (<10km depth). Temperature was estimated by several geothermometers, which yielded crystallization temperatures ranging from 835º to 958ºC for the gabbros, and from 665º to 862ºC for the diorites. Field, petrological, geochemical and mineralogical characteristics of the SLMI are akin to the Egyptian layered mafic-ultramafic intrusions of volcanic-arc setting, not ophiolitic rocks.

KEYWORDS | **Neoproterozoic. Arabian-Nubian Shield. Sinai. Layered mafic intrusion. Volcanic-arc.**

INTRODUCTION

The basement rocks of Egypt represent the northwestern part of the Arabian-Nubian Shield (ANS). It was separated from the eastern portion in Saudi Arabia during the formation of the Red Sea and related structures such as the Gulf of Suez and the Gulf of Aqaba. The Neoproterozoic juvenile crust of the ANS consists of a collage of volcanic-arc terranes and the associated ophiolite remnants, which were amalgamated during the assembly of Gondwana (Ali *et al*., 2010; Genna *et al*., 2002; Johnson and Woldehaimanot, 2003; Meert, 2003; Stoeser and Frost, 2006). The ANS forms the northern continuation of the Mozambique belt that has been referred to as the East African Orogen (*e.g*. Patchett and Chase, 2002; Stern, 1994).

There are three tectonic events during the Neoproterozoic evolution of the northern ANS. The first (ca. 820 and 720Ma) has been considered to represent the age of ophiolite obduction and island arc terrane accretion (Ali *et al*., 2010; Kröner *et al*., 1994; Stern, 1994, 2002). The second (ca. 620 and 650Ma) has been interpreted as a probable collisional stage during which the accreted juvenile terranes attached to the East Saharan Craton (Kröner *et al*., 1994; Schandelmeier *et al*., 1987). The third stage has been considered as a post-collisional phase. During the post-collisional phase widespread calc-alkaline (630-590Ma) and alkaline (610-580Ma) magmatism intruded the northern part of the ANS, pointing to their coeval generation between 610 and 590Ma (Avigade and Gvirtzman, 2009; Azer *et al*., 2010; Be'eri-Shlevin *et al*., 2009; Beyth *et al*., 1994; Eyal *et al*., 2010). The mafic-ultramafic complexes are widespread in several tectono-stratigraphic units of the ANS. They represent parts of Neoproterozoic ophiolitic rocks and members in mafic-ultramafic intrusions of subduction related and post-orogenic younger mafic-ultramafic layered intrusions. The mafic-ultramafic rocks represent important elements for reconstructing the geodynamic evolution of the ANS and other Neoproterozoic orogenic belts.

Precambrian mafic-ultramafic plutonic rocks of Egypt have different ages and tectonomagmatic evolution. They were classified into older and younger rocks (*e.g*. Takla *et al*., 1981). The older mafic-ultramafic rocks form an integral part of obducted ophiolitic sequences (El-Sayed *et al*., 1999; El Sharkawy and El Bayoumi, 1979; Takla *et al*., 1981) or constitute members of subduction-related, calc-alkaline gabbro-diorite complexes (Abu El-Ela, 1996, 1997; El-Gaby *et al*., 1988, 1990). The younger mafic-ultramafic suites are mostly fresh, undeformed and unmetamorphosed (Azer and El-Gharbawy, 2011; Basta, 1998; El-Gaby *et al*., 1990; Takla *et al*., 1981). They were considered as post-orogenic rocks (Azer *et al*., 2012; El-Ramly, 1972; Ghoneim *et al*., 1992; Takla *et al*., 1991).

The mafic-ultramafic rocks are very limited in Sinai Peninsula and the previous studies on these rocks created a considerable controversy on their tectonic setting, origin and age. The Shahira Layered Mafic Intrusion (SLMI) is the oldest layered mafic intrusion in south Sinai (~632±4Ma; Be'eri-Shlevin *et al*., 2009). The tectonic setting of this intrusion is controversial and its evolution in relation to south Sinai basement rocks is still a matter of debate. A range of tectonic settings have been proposed for the SLMI: from ophiolitic to continental settings (Abdel Khalek *et al*., 1994; Aly and El Baraga, 1997; Basta, 1998; El-Gharbawy and Hassen, 2001; Furnes *et al*., 1985; Hassanen, 1989; Moghazi *et al*., 1998; Shimron, 1981; Takla *et al*., 2001). Also, Be'eri-Shlevin *et al*. (2009) and Eyal *et al*. (2010) assigned this intrusion to the onset of post-collisional magmatism. This paper aims to better understand the petrogenetic and geotectonic history of the SLMI. Consequently, we have combined all the gained information on its field relationships, petrography and mineralogy as well as the geochemistry data. Also, the obtained results were compared with the available geological and geochemical data of the mafic rocks from the ANS.

GEOLOGICAL BACKGROUND

Regional geology

The Precambrian rocks of south Sinai constitute the extreme northern end of the ANS (Fig. 1A). The basement rocks of Sinai consist essentially of remnants of older metamorphic complexes engulfed by large volumes of younger mostly non-metamorphosed granitic intrusions. The metamorphic rocks in Sinai are grouped into five metamorphic complexes: the Feiran-Solaf, Sa'al-Zaghra, Kid, Watir and Taba (Fig. 1A); smaller areas of metamorphic rocks are scattered throughout the Sinai massif. They consist of schists, migmatites and gneisses and the metamorphism ranges from greenschist to amphibolite facies (*e.g*. Abu El-Enen *et al*., 2004; Eyal, 1980; Eyal and Amit, 1984).

Mafic plutonic rocks constitute only a small fraction of south Sinai batholiths (Fig. 1A). Ultramafic rocks are very rare and represented only by a small body of serpentinite, ~200m^2, and intruded (Madbouly, 1991; Moussa, 2002) or tectonically emplaced over the migmatites and gneisses at the Kabr El-Bonaya in the Wadi Kid area (Abu El-Enen and Makroum, 2003; Beyth *et al*., 1978; Shimron, 1981). Post-tectonic ultramafic peridotites are reported from the Imleih layered intrusion in relation with gabbros (Azer and El-Gharbawy, 2011).

The SLMI is located within the Kid metamorphic complex. The late Neoproterozoic rocks of Wadi Kid

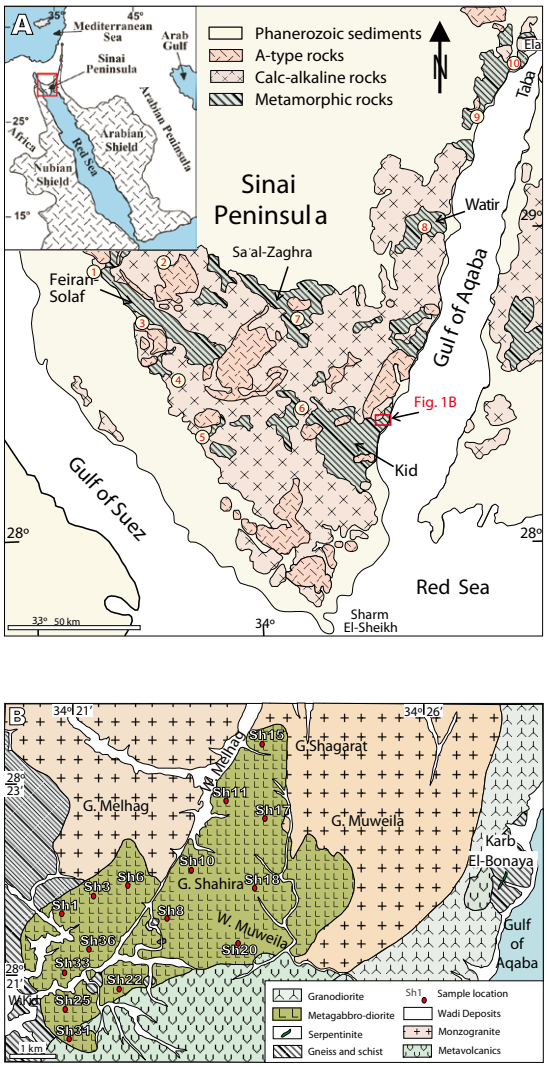

FIGURE 1. A) Geological map of southern Sinai, Egypt (modified after Eyal *et al.*, 1980) with inset of the Arabian-Nubian Shield (ANS), location of Figure 1B and major late Neoproterozoic gabbroic intrusions in southern Sinai are indicated: 1) Nasrin, 2) Imleih, 3) Rimm, 4) Hibran-Mi,ar, 5) Imlaha, 6) Sheikh El-Arab, 7) Sa'al-Zaghra, 8) Nakhil, 9) El-Mahash and 10) Tweiba areas; and B) Simplified geological map of Gabal Shahira area, south Sinai (modified after Madbouly, 2000).

area comprise metamorphic rocks, volcano-sedimentary successions, gabbro-diorite rocks and granite intrusions, as well as very small ultramafic masses at the Kabr El-Bonaya area (Azer *et al.*, 2010; Furnes *et al.*, 1985; Shimron, 1980, 1984). The metamorphic rocks in the Kid area include gneisses, schists, metavolcanics and metasediments. They represent an island arc stage (Eyal *et al.*, 2014; Furnes *et al.*, 1985; Shimron, 1980) that underwent polyphase deformation (Khalaf and Obeid, 2013). Metamorphic grades range from lower-greenschist to amphibolite facies with a general increase of grade towards the central and northern parts of the area (Abu El-Enen, 2008; Brooijmans *et al.*, 2003; Furnes *et al.*, 1985). The available U-Pb ages of zircons in the Kid arc ranges between 640 and 620Ma (Eyal *et al.*, 2014), while Moghazi *et al.* (2012) obtained a higher age for this stage (715-890Ma). Low U-Pb ages for the Kid arc reflect Pb loss during deformation and metamorphism.

The Kid metavolcanics have compositions various from andesite to rhyolite. They have been formed in an oceanic island arc (El-Metwally *et al.*, 1999; Eyal *et al.*, 2014; Furnes *et al.*, 1985; Shimron, 1980). They are similar to the calc-alkaline metavolcanics in the Eastern Desert of Egypt (Stern, 1981). El-Gaby *et al.* (1991) and Moghazi (1994) suggested that the Kid metavolcanic sequence may correlate with the subaerial calc-alkaline Dokhan-type volcanics of the Eastern Desert of Egypt. El-Bialy (2010) suggested that the volcanic rocks of Wadi Kid area are post-collision extrusives formed during extensional tectonics. Zircons from rhyolite clasts in the Kid area define a $^{206}Pb/^{238}U$ weighted mean age of 609 ± 5Ma, which was considered as the approximate age of volcanism (Moghazi *et al.*, 2012). This age is comparable with the post-collisional Dokhan-type volcanics in south Sinai (Be'eri-Shlevin *et al.*, 2011).

The Kid metasediments were deposited in a deep water environment (Shimron, 1980) and show well bedding, fining-upward and laminated successions of porphyroblastic schists interbedded with metacalcpelites enclosing marble lenses and quartzites (Shimron, 1980). There are turbidities, with diagnostic sedimentary structures, such as fining-up sequences (Brooijmans *et al.*, 2003). Bielski (1982) and Halpern and Tristan (1981) obtained whole rock Rb-Sr isochron age of 610-616Ma for the metasediments and metavolcanics of Kid area. Also, Moghazi *et al.* (2012) obtained a weighted mean $^{206}Pb/^{238}U$ age of 615 ± 6Ma for Kid metasediments. The obtained ages for the kid metasediments are low and thus can interpret to reflect Pb loss during deformation and metamorphism.

The plutonic rocks of the Kid area include a layered mafic intrusion and various granitic bodies (Azer *et al.*, 2010; Moghazi *et al.*, 1998; Shahien, 2002). The SLMI and ultramafics of the Kabr El-Bonaya (located to the east of the SLMI, Fig. 1B) were named as Dahab ultramafics and considered to be an ophiolite suite (Abdel Khalek *et al.*, 1994; Abu El-Enen and Makroum, 2003; Beyth et al, 1978; Shimron, 1981, 1984). Most of the granitic rocks are broadly A-type alkaline plutons (Be'eri-Shlevin *et al.*, 2009; Eyal *et al.*, 2010, 2014), including monzogranite, syenogranite and albitite. The available zircon U-Pb ages of the granitic rocks of the Kid area range from 604 to 607Ma (Azer *et al.*, 2010; Be'eri-Shlevin *et al.*, 2009; Moghazi *et al.*, 2012), which represent the crystallization age of the magma.

Local geology

The SLMI is located north of the Wadi Kid, about 25Km south of Dahab City on the western side of the Gulf of Aqaba. It lies between latitudes 28º 20' 15" and 28º 24' 05"N and longitudes 34º 20' 45" and 34º 25' 50"E (Fig. 1B).This layered mafic intrusion is the largest gabbroic mass in south Sinai (~20km^2) and occurs as a single large intrusive body in the Kid Metamorphic complex. The SLMI forms an irregular mass of moderate to high relief showing NNE elongation. It intrudes the metamorphic rocks in the mapped area and they are intruded by the post-orogenic granites. The metavolcanic rocks of Wadi Kid area (Fig. 1B) are intercalated with metasediments (Abdel Khalek *et al.*, 1994; Bogoch and Magaritz, 1983; Hassanen, 1989; Moghazi *et al.*, 2012; Shimron, 1980). The contact between the SLMI and the metavolcanics are sharp. Field relations indicate that the Shahira gabbros intruded the lower succession of the metavolcanics, while it is unconformably overlain by the upper succession of these volcanics. The SLMI is intersected from the west by a major fault trending NNE. The Shahira gabbros are medium- to coarse-grained, ranging in color from dark to light greenish grey and characterized by spheroidal weathering. The outer zone of the intrusion is fine-grained gabbro, which possibly represents a chilled margin. Fine-grained gabbro occurs only in the southern and western parts of the layered intrusion along contacts against the metamorphic rocks.

The Shahira mafic intrusion includes layered and massive gabbroic rocks. The former includes pyroxene-hornblende gabbro and hornblende gabbro, while the later includes hornblende gabbro and diorite. The pyroxene-hornblende gabbro is less abundant than the hornblende gabbro. Layering in the SLMI is observed in some exposures, especially in the western and central parts of the intrusion. Layering appears to imply repeated injection of new magma or cyclic variation in physical properties. The layer thicknesses vary from few centimeters to up to 1.5 meter thick and are dislocated due to the effect of faulting. Few pockets of pegmatitic gabbro and pyroxenite are observed. These pockets are concordant with general layering of the intrusion, and represent gabbroic segregation in the last stage of magma evolution before crystallization of diorites.

The dioritic rocks of the SLMI are less common than gabbro varieties. They are well exposed in the southern part of the intrusion at the top of the gabbro and close to the contact with the schist. Contacts between gabbros and diorites are transitional and poorly discerned in the outcrops. They can only be recognized by the slightly lighter color of the rocks. Several gabbro offshoots are recorded near contacts within the metamorphic country rocks. Few xenoliths of gneisses are observed within the gabbro near the contacts with the metamorphic country rocks. The diorites contain few small, rounded fine-grained xenoliths or mafic microgranular enclaves of gabbro composition. Apophyses of granites show considerable variation in color and texture extend into the gabbros. Adjacent to the granite intrusions, the gabbros are characterized by heavy hydrothermal alteration; the degree of alteration generally decreases away from the granite intrusion. In some outcrops, the gabbroic rocks are deformed, especially near the contact with the granites. The gabbro massif is intruded by many dykes of different compositions which increase northwards and trending NE.

The SLMI was dated at 632±4Ma by using ion-probe U-Pb dating of zircon (Be'eri-Shlevin *et al.*, 2009); this age represents the crystallization age of the magma. The obtained age is reliable since the SLMI was intruded by granites with ages ranging between 590 and 610Ma (U-Pb dating of zircon, Be'eri-Shlevin *et al.*, 2009).

PETROGRAPHY

Based on petrographic and mineralogical studies, the SLMI is distinguished into: fine-grained gabbro, pyroxene-hornblende gabbro, hornblende gabbro and diorite to quartz-diorite. The petrographic descriptions of each rock unit of the studied layered mafic intrusion are given below.

Fine-grained gabbro (chilled margin)

The fine-grained gabbro has sub-ophitic to granular textures, being composed mainly of plagioclase (51-63vol.%), brown hornblende (27-30vol.%), pyroxenes (3-6vol.%), opaques (4-8vol.%) and rare olivine, together with accessory biotite and apatite. It has the same mineralogical composition as the pyroxene-hornblende gabbro (described below). Plagioclase occurs as large crystal aggregates or as small laths enclosed in the brown hornblende. The hornblende occurs as fresh crystals or locally altered to biotite, actinolite and chlorite. Both orthopyroxene and clinopyroxene were observed in the fine-grained gabbro as minor components (Fig. 2A). Clinopyroxene occurs as euhedral to subhedral crystals of augite which are partially transformed into amphiboles. Enstatite represents orthopyroxene and occurs as anhedral crystals. Olivine occurs as small crystals within the plagioclase (Fig. 2B) or as interstitial fine-grained crystals among other constituents.

Pyroxene-hornblende gabbro

The pyroxene-hornblende gabbro is coarse-grained, equigranular and melanocratic rock. It exhibits poikilitic

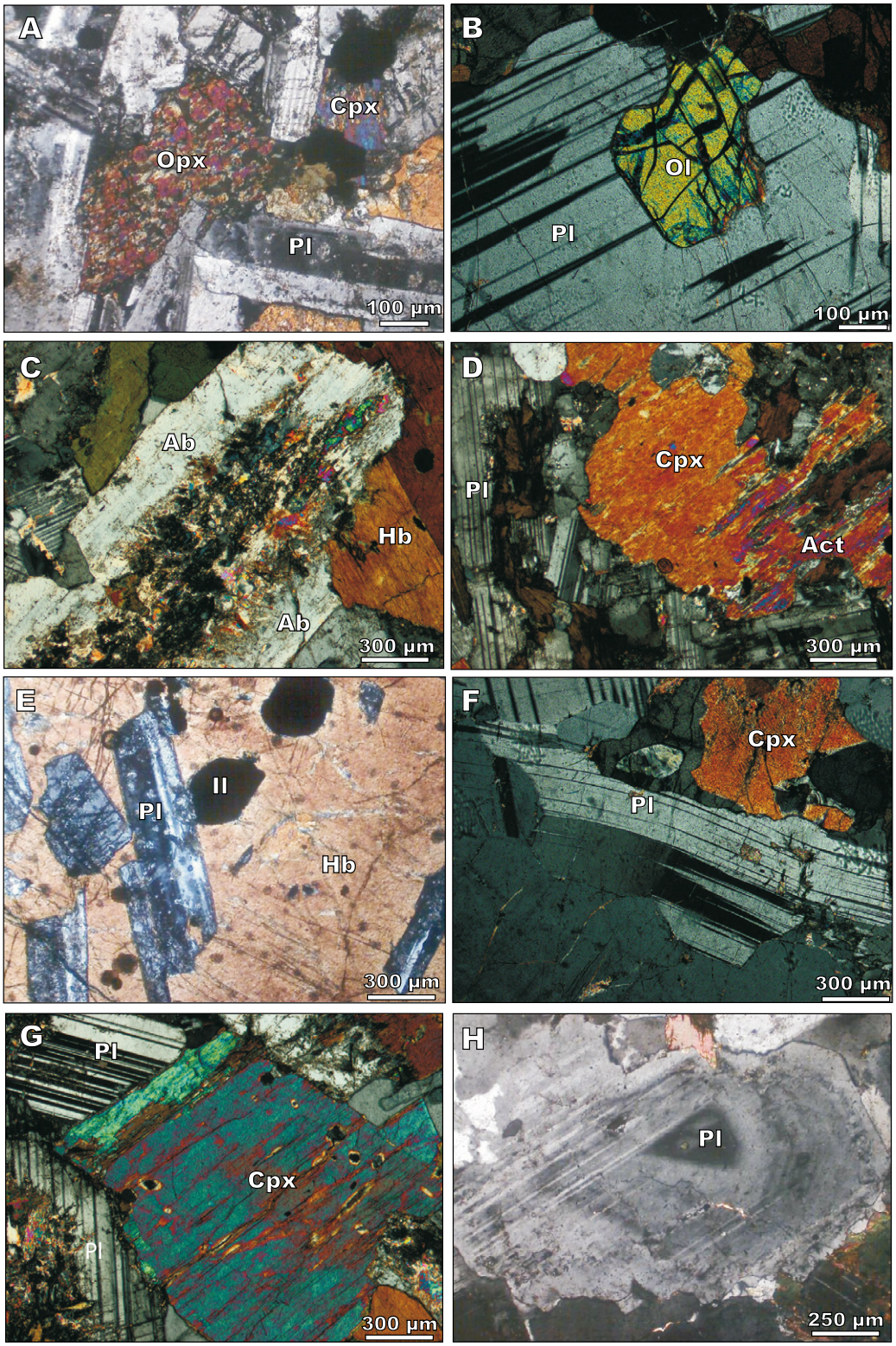

FIGURE 2. Microphotographs of the Shahira Layered Mafic Intrusion (SLMI). A) Orthopyroxene and clinopyroxene in the fine-grained gabbro, B) olivine crystal enclosed within plagioclase in the fine-grained gabbro, C) saussuritized plagioclase replaced by albite and epidote in the pyroxene-hornblende gabbro, D) secondary amphibole (actinolite) replacing clinopyroxene in the pyroxene-hornblende gabbro, E) hornblende showing numerous inclusions of plagioclase laths and ilmenite, resulting in the poikilitic texture of the pyroxene-hornblende gabbro, F) deformed crystal of plagioclase with kink bands in the hornblende gabbro, G) subhedral clinopyroxene crystal in the hornblende gabbro, and H) oscillatory zoning in the plagioclase crystal of the diorite. Mineral abbreviations are: Ol= olivine, Cpx= clinopyroxene, Opx= orthopyroxene, Hb= hornblende, Act= actinolite, Il= ilmenite, Pl= plagioclase and Ab= albite.

texture and is essentially composed of plagioclase (53-65vol.%), amphiboles (27-33vol.%), augite (3-6vol.%) and opaques (4-7vol.%) with rare orthopyroxene crystals were observed. Biotite, titanite and apatite are accessory phases. Plagioclase occurs as subhedral to anhedral crystals and few crystals are zoned. Some plagioclase crystals are saussuritized and rarely replaced by albite and epidote (Fig. 2C), especially crystal cores. Primary and secondary amphiboles can be observed in the pyroxene-hornblende gabbro. The secondary amphiboles substitute primary amphiboles and clinopyroxene (Fig. 2D). The primary amphiboles are mainly represented by hornblende, which includes numerous inclusions of plagioclase laths and ilmenite resulting in a poikilitic texture (Fig. 2E). Clinopyroxene is represented mainly by augite and partly altered to actinolite.

Hornblende gabbro

The hornblende gabbro constitutes the main part of the intrusion, being medium- to coarse-grained with ophitic to subophitic texture, and composed mainly of plagioclase (50-66vol.%) and hornblende (28-354vol.%), with rare biotite (1vol.%) and clinopyroxene (~1vol.%). Accessory minerals include Fe-Ti oxides and apatite. The majority of the plagioclase crystals are subhedral, and the large crystals are usually zoned. Saussuritization is observed in some plagioclase cores. Hornblende represents the main ferromagnesian minerals and occurs as large plates enclosing plagioclase, opaques and apatite, giving poikilitic texture. It is fresh, but partly altered to actinolite and iron oxides. Few crystals of plagioclase are deformed with kink bands (Fig. 2F). Clinopyroxene occurs as subhedral crystals in the interstices of large plagioclase laths (Fig. 2G).

Diorite and quartz-diorite

The diorite generally exhibits medium-grained intergranular textures. It consists mainly of plagioclase (55-67vol.%), mafic minerals (14-27vol.%), quartz (<6vol.%) and alkali-feldspar (<4vol.%), with accessory apatite, zircon and opaque minerals. Plagioclase is the most common mineral and occurs as subhedral tabular crystals, which show normal and rarely oscillatory zoning (Fig. 2H). Some plagioclase crystals are corroded indicating disequilibrium conditions. Mafic minerals comprise hornblende and biotite in variable proportions. Biotite is reddish-brown and forms discrete anhedral to subhedral flakes associated with amphibole. K-feldspar occurs as few subhedral to anhedral crystals between plagioclase. Quartz presents as interstitial grains with sutured outlines.

Quartz-diorite exhibits medium-grained hypidiomorphic texture. It consists of plagioclase (60-65vol%), hornblende (15-20vol%), K-feldspars (2-6vol%), biotite (2-4vol%), quartz (5-10vol%) and opaques (2-3vol%). Plagioclase is the most common mineral and presents as subhedral tabular crystals; some crystals show normal zoning. K-feldspar occurs as subhedral to anhedral grains between plagioclase crystals. Hornblende occurs as anhedral tabular crystals, and usually contains inclusions of Fe-Ti oxides and zircons. Biotite occurs as discrete anhedral to subhedral crystals. Quartz occurs as anhedral interstitial grains and shows undulatory extinction with sutured outlines.

The mafic microgranular xenoliths enclosed within the dioritic rocks are fine-grained rocks of gabbroic composition. They consist mainly of plagioclase, biotite and hornblende. The accessory minerals include opaques and apatite. Some large plagioclase xenocrysts show a spongy cellular texture due to dissolution by the host diorite hydrous magma.

ANALYTICAL METHODS

Chemical compositions of primary magmatic and secondary minerals from the SLMI were determined using a CAMECA CAMEBAX SX-50 Electron Probe Micro Analyzer (EPMA) housed at the Bureau de Recherches Géologiques et Minières (BRGM), Orléans, France. Mineral chemical analyses were performed under operating condition of 15kV accelerating voltage and 20nA beam current. Suitable synthetic and natural standards were applied for calibration. The whole dataset of mineral chemistry are listed (Tables I-VI Electronic Appendix, available at www.geologica-acta.com).

Fifteen representative samples covering the main lithologies of the SLMI were selected for bulk chemical analyses. Whole-rock chemical analyses of powdered rock samples from the study rocks were carried out at ACME Analytical Laboratories (Canada) for major oxides, trace elements and Rare Earth Elements (REE) (Tables 1; 2). Major oxides compositions and Ba, Co, Cu, Nb, Ni, Sc, Sr, Y, Zn, and Zr elements were analyzed using Inductively Coupled Plasma-Emission Spectrometry (ICP-ES). The rest of trace elements and the REE were determined using Inductively Coupled Plasma-Mass Spectrometry (ICP-MS) following a lithium metaborate/tetraborate fusion and nitric acid digestion of a 0.2g sample. Analytical precision, as calculated from replicate analyses, is 0.5% for major element and varies from 2% to 20% for trace element.

MINERAL CHEMISTRY

Olivine

Few olivine crystals are present in the fine-grained pyroxene-hornblende gabbro (sample No. Sh3, chilled

margin). Microprobe analyses of olivine and their calculated structural formulae are shown in Table I. Olivines have narrow content ranges of SiO_2 (38.22-39.47wt.%), FeO (15.82-17.35wt.%) and MgO (43.28-44.87wt.%) contents. They have low MnO (<0.24wt.%) and CaO (<0.01wt.%) contents. Fo content of the analyzed olivine crystals range from 82 to 83%, with an average of 82. The NiO contents of the analyzed olivines (<0.15wt.%) are lower than those of the mantle olivine array (Takahashi *et al.*, 1987), but similar to the Egyptian layered mafic intrusions (Fig. 3A).

Pyroxenes

Results of both orthopyroxene (opx) and clinopyroxene (cpx) from the SLMI are presented in Table II. All analyzed orthopyroxene is included in the samples from fine-grained gabbro (chilled margin). It shows a composition close to enstatite end-member of Morimoto *et al.* (1988). The enstatite analyses show narrow change in its composition (Wo_{1-3} En_{80-84} Fs_{14-18}). Mg# [(Mg/(Mg+Fe^{+2})] ranges between 0.82 and 0.86 with an average value of 0.83.

The clinopyroxenes of the fined-grained gabbro (chilled margin) and hornblende gabbro were analyzed. They show very narrow compositions (Wo_{45-48} En_{40-42} Fs_{11-13} in the fine-grained gabbro and Wo_{45-48} En_{39-42} Fs_{11-14} in the hornblende gabbro) and plot across the augite-diopside boundary according to the classification given by Morimoto *et al.* (1988). The clinopyroxenes have low Al_2O_3 (<1.56%), TiO_2 (<0.16%) and Na_2O (<0.33%) and Mg# ranges from 0.75 to 0.86, with an average of 0.81. Le Bas (1962) used a SiO_2 *versus* Al_2O_3 diagram for clinopyroxene to discriminate magma alkalinity between mafic magma series. All the clinopyroxene analyses from the fine-grained gabbro and hornblende gabbro plot in the subalkaline field of such diagram (Fig. 3B).

Biotite

Biotite from the quartz-diorite samples was analyzed and its chemical compositions and structural formula are given in Table III. The analyzed biotite crystals are iron-rich with FeO*/MgO ratio ranging from 1.23 to 1.59, with an average 1.31. They mostly show the chemical characteristics of primary igneous biotites (Fig. 3C) which composition can reflect the nature of their host magmas (Abdel-Rahman, 1994). The average of FeO*/MgO ratio (1.31) of the analyzed biotites is very similar to that of calc-alkaline, orogenic biotites (av. 1.76, Abdel-Rahman, 1994). Using the Al_2O_3 *versus* $FeO_{(t)}$ biotite discrimination diagram, the biotite analyses plot in the field of calc-alkaline orogenic suite (Fig. 3D).

Amphiboles

The analyzed amphiboles are representative to the fine-grained gabbro (chilled margin), the hornblende gabbro and the quartz-diorite. Chemical analyses of the amphiboles are shown in Table IV. The amphibole crystals include primary and secondary amphiboles. The primary amphiboles are high in Al_2O_3 (9.57–11.77wt.% in the fine-grained gabbro, 9.55-11.23wt.% in the hornblende gabbro and 5.93–8.91wt.% in the quartz-diorite) and TiO_2 (2.34–3.95wt.% in the fine-grained gabbro, 2.38–4.03wt.% in the hornblende gabbro and 1.11–1.96wt.% in the quartz-diorite). In contrast, the secondary amphiboles have low Al_2O_3 (1.04–6.53wt.%) and TiO_2 (0.03–0.99wt.%) contents. All the analyzed amphiboles are calcic in composition according to the classification scheme of Leake *et al.* (1997), with Ca ranging from 1.62 to 2.11a.p.f.u (atoms per formula unit). The primary amphiboles in the fine-grained gabbro and hornblende gabbro include magnesio-hornblende, tschermakitic hornblende and magnesio-hastingsite, while in the quartz-diorite represented by magnesio-hornblende. Magnesio-hornblende and actinolite/tremolite represent secondary amphiboles in the SLMI rocks.

Feldspars

Chemical compositions and structural formulae of the feldspar crystals are given in Table V. The analyzed feldspars in the fine-grained gabbro (chilled margin) are mainly represented by labradorite (An_{52-70}) and rarely albite (An_{1-8}) and andesine (An_{43-47}).Whereas in the hornblende gabbro, they are mainly andesine (An_{35-42}) and rarely albite (An_{5-8}) and labradorite (An_{56-66}). Feldspars in the quartz-diorite include plagioclases and K-feldspar. The plagioclases are less calcic than those of gabbros and are mainly oligoclase (An_{22-27}) and andesine ($An3_{1-44}$). The zoned plagioclase crystals have high An-content (57.8–59.4%) cores surrounded by low An-content rims (27.0–32.9%). K-feldspar in the quartz-diorite is almost pure orthoclase (Or_{94-98}).

Fe-Ti oxides

Chemical compositions of the Fe-Ti oxides are shown in Table VI. The analyzed Fe-Ti oxides of the SLMI samples include magnetite and ilmenite. In general, the analyzed magnetites have very low-TiO_2 content (<0.63wt.%). End-member components (X_{ilm}) of ilmenite are calculated according to Stromer (1983). The ilmenite of the hornblende gabbro is nearly pure (95–100% ilmenite mole) and enriched in MnO content (up to 1.76wt.%) relative to the magnetite (up to 0.2wt.%). The ilmenite from the quartz-diorite contains 90-96% ilmenite mole and has between 1.65-2.48wt.% MnO. The high MnO contents in ilmenite is due to simple substitution of Mn for Fe^{2+} with

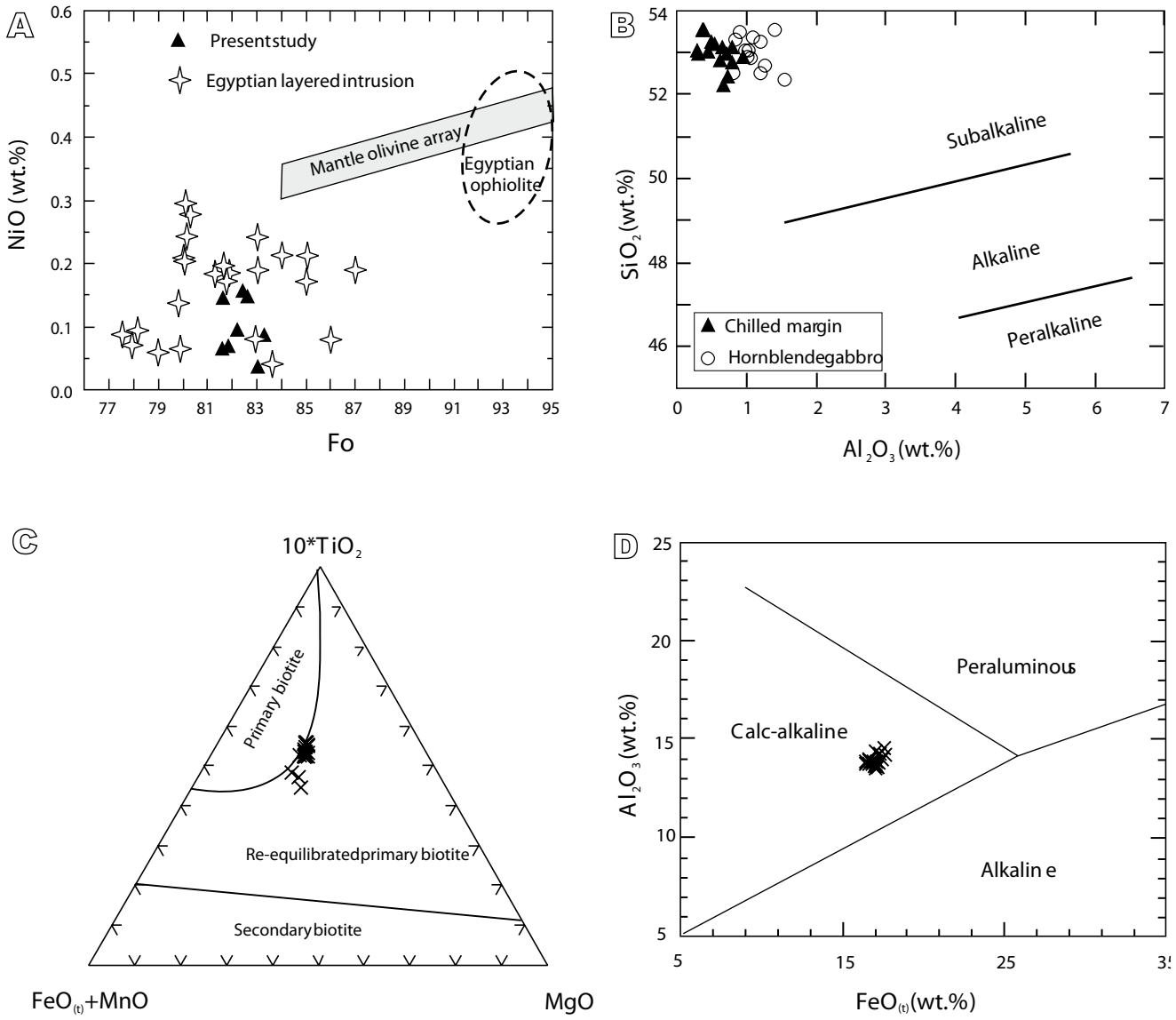

FIGURE 3. A) Variation of NiO (wt.%) and Fo content in the olivines of the SLMI. The field of mantle olivine array is adopted from Takahashi *et al.* (1987), whereas the fields of the Egyptian ophiolite and layered mafic intrusions draw based on the published data (Abd El-Rahman *et al.*, 2012; Ahmed, 2013; Ahmed *et al.*, 2008; Essawy *et al.*, 1997; Khedr and Arai, 2013; Khudeir, 1995a, b). B) SiO_2-Al_2O_3 discrimination diagram of clinopyroxenes in the gabbroic samples (Le Bas, 1962). C) TiO_2-($FeO_{(t)}$+MnO)-MgO ternary diagram for the biotite of Shahira quartz-diorite (Nachit *et al.*, 2005). D) $FeO_{(t)}$ *vs.* Al_2O_3 biotite discriminant diagram for the analyzed biotites (Abdel-Rahman, 1994).

increasing oxygen fugacity under magmatic conditions to form pyrophanite ($MnTiO_2$) (Deer *et al.*, 1992)

GEOCHEMICAL CHARACTERISTICS

The geochemical analyses and calculated normative minerals of different rock units in the SLMI are given in Table 1. The normative mineral compositions are calculated using Minpet Software (Richard, 1995). Based on the normative compositions of the analyzed samples, the fine-grained gabbro (chilled margin) has the highest color index (36–38), while the quartz-diorites have lowest color index (18–22). The hornblende gabbro and diorites are quartz normative, and the fine-grained gabbro and pyroxene-hornblende gabbro are olivine normative (Table 1). The analyzed samples have a wide composition range with respect to their silica content (42.07 to 57.75 SiO_2 wt.%). They plot within the gabbro and diorite fields (Fig. 4A, B). The samples of fine-grained gabbro do not fall in the TAS gabbro field because they are depleted in silica. The chemical compositions of the SLMI are consistent with their mineralogical compositions. The fine-grained gabbro has the highest contents of MgO (8.6–9.24wt.%), Ni (68–71ppm), Cr (185–214ppm) and Co (59–61ppm), suggesting pristine magma composition. The dioritic rocks are distinguished from the pyroxene-hornblende gabbro and hornblende

gabbro by their relatively high Na_2O (3.07–3.83wt.%) and K_2O (1.57–2.29wt.%), and low MgO (2.94–4.94wt.%), Fe_2O_3 (5.65–8.01wt.%), Ni (26–44ppm), Cr (47–99ppm) and Co (20–30ppm) content. The fine-grained gabbro has the highest Mg# (63.8–64.2), while the diorites have the lowest Mg# (54.2–59.0). The pyroxene-hornblende gabbro has higher Mg# (60.9–63.3) than the hornblende gabbro (58.5–61.7) and the diorites (54.2–59.0).

In the SiO_2 *versus* alkali (Na_2O+K_2O) diagram (Fig. 4A), the different rock units of the SLMI plot in the sub-alkaline field using the dividing line of Miyashiro (1978). They show calc-alkaline affinity in the Co *versus* Th classification diagram (Fig. 4B) of Hastie *et al*. (2007) and in the SiO_2-MgO *versus* Al_2O_3/TiO_2 diagram (Fig. 4C) of Middlemost (1997). In the variation diagrams (Figs. 5; 6), TiO_2, Fe_2O_3, MgO, CaO, Co, Ni and Cr have negative correlation trends, whereas K_2O+Na_2O, Rb, Nb, Y, Th, Hf and Zr display positive correlation trends with SiO_2 suggesting that these rocks may be evaluated through fractional crystallization processes. The Sr content increase from the pyroxene-hornblende gabbro to hornblende gabbro and then decrease in diorites. These systematic compositional variations imply that differentiation of plagioclase, pyroxene, amphibole and Fe-Ti oxides played an important role in the evolution of the studied layered mafic intrusion.

MORB mantle-normalized patterns for the various rock units of the SLMI are generally similar (Fig. 7A). They show significant enrichment in the LILE (K, Rb, Ba) over HFSE (Nb, Zr, Hf, Ti, Y) with slightly depletion in Ta-Nb relative to the neighboring LILE, similar to typical volcanic-arc signature (Hollings and Wyman, 1999).

REE analyses of 15 samples of the SLMI are provided in Table 2 and their chondrite-normalized REE patterns are represented in Figure 7B. Diorite and quartz-diorite have higher ΣREE (105–150ppm) contents than gabbros (53–93ppm). REE patterns for the SLMI have enriched LREE relative to HREE [$(La/Yb)_n$= 4.5–8.2]. The gabbro samples are characterized by slightly positive to negative Eu-anomalies [$(Eu/Eu^*)_n$= 0.93–1.09], while the diorite and quartz-diorite samples display slightly negative Eu-anomaly [$(Eu/Eu^*)_n$= 0.74–0.85].

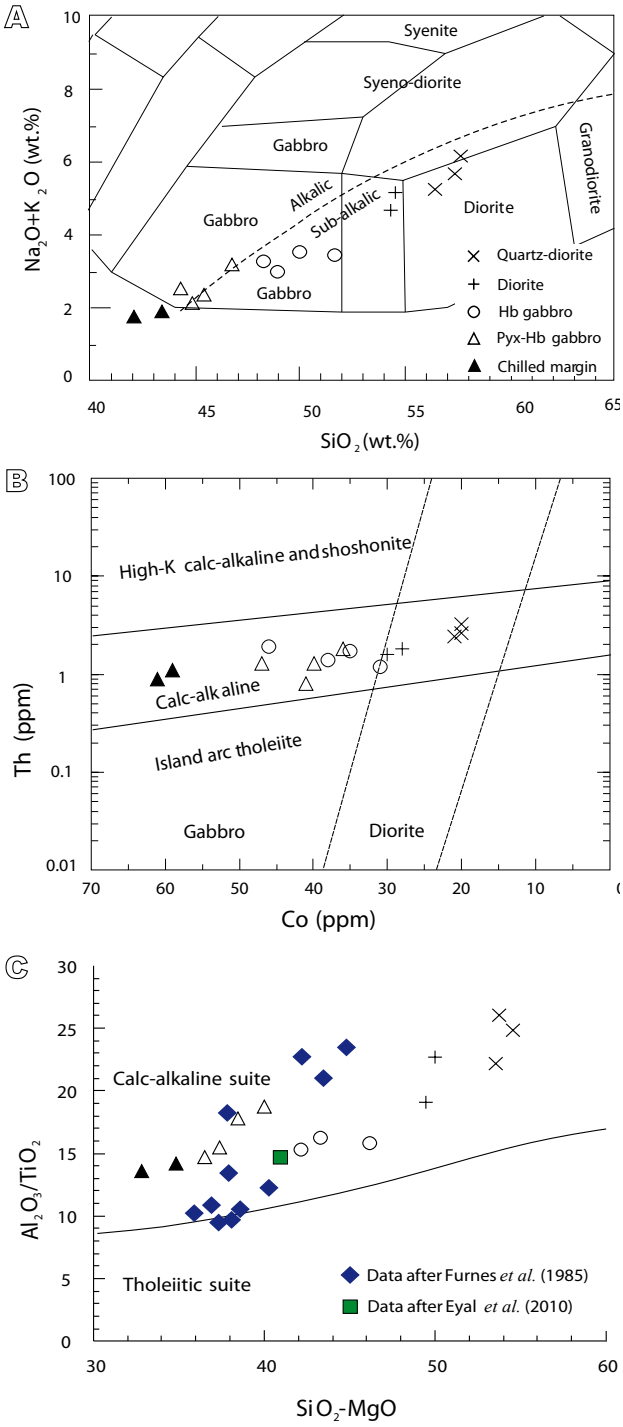

FIGURE 4. A) TAS diagram for the SLMI (Cox *et al.*, 1979; adapted by Wilson, 1994). The dividing dashed line between alkalic and sub-alkalic magma series is from Miyashiro (1978), B) Th *vs.* Co classification diagram (after Hastie *et al.*, 2007) for the SLMI, and C) Al_2O_3/TiO_2 *versus* SiO_2-MgO diagram to separate subalkalic basic and intermediate rocks into tholeiitic and calc-alkaline lineages (after Middlemost, 1997). The Shahira gabbro data of Furnes *et al.* (1985) and Eyal *et al.* (2010) are plotted for comparison.

THE PHYSICO-CHEMICAL CONDITIONS OF MAGMA CRYSTALLIZATION

Geothermobarometry

Pyroxene, biotite, plagioclase, hornblende and Fe-Ti oxides can be used to indicate variations in the chemistry of magma and determine its P-T conditions (Blundy and Holland, 1990; Lindsley, 1983; Ridolfi *et al*., 2010; Schmidt, 1992; Stromer, 1983). The application of the various

TABLE 1. Major and trace element contents as well as the normative compositions of the Shahira layered gabbro intrusion

Rock type	Chilled margin		Pyroxene-hornblende gabbro				Hornblende gabbro				Diorite		Quartz-diorite		
Sample No.	Sh1	Sh3	Sh6	Sh11	Sh15	Sh17	Sh8	Sh10	Sh18	Sh20	Sh22	Sh25	Sh31	Sh33	Sh36
Major oxides (wt.%)															
SiO_2	42.07	43.41	45.41	44.87	44.30	46.77	51.71	48.98	50.02	48.30	54.40	54.60	57.75	57.43	56.51
TiO_2	1.40	1.37	1.08	1.24	1.29	1.04	1.09	1.16	0.98	1.17	0.88	0.72	0.68	0.64	0.82
Al_2O_3	19.03	19.44	19.20	19.21	18.92	19.46	17.22	18.80	16.53	17.91	16.83	16.32	16.90	16.66	18.16
Fe_2O_3	12.21	11.19	10.07	10.56	10.51	10.13	9.19	8.23	9.62	8.93	8.01	7.95	5.65	6.50	5.79
MnO	0.14	0.16	0.11	0.10	0.14	0.14	0.12	0.13	0.17	0.15	0.14	0.14	0.09	0.12	0.11
MgO	9.24	8.60	6.94	7.47	7.78	6.76	5.55	5.68	5.86	6.18	4.94	4.62	3.18	3.67	2.94
CaO	10.76	10.14	11.16	10.17	10.37	11.07	8.63	11.28	10.05	9.90	8.07	7.24	6.19	6.19	6.56
Na_2O	1.35	1.43	1.68	1.52	1.83	2.44	2.32	2.21	2.29	2.32	3.07	3.34	3.83	3.71	3.43
K_2O	0.38	0.44	0.65	0.57	0.66	0.72	1.08	0.75	1.20	0.92	1.57	1.78	2.29	1.93	1.80
P_2O_5	0.24	0.50	0.17	0.79	0.69	0.07	0.24	0.13	0.15	0.41	0.25	0.20	0.30	0.28	0.29
LOI	2.05	2.68	2.62	2.54	2.64	1.23	2.07	1.73	2.34	2.64	1.49	1.89	2.31	1.87	2.54
Total	98.87	99.36	99.09	99.04	99.13	99.83	99.22	99.08	99.21	98.83	99.65	98.80	99.17	99.00	98.95
Mg#	63.82	64.18	61.63	62.25	63.31	60.87	58.47	61.67	58.68	61.73	58.98	57.53	56.75	56.82	54.20
Trace elements (ppm)															
Cr	214	185	147	142	156	97	68	123	85	115	87	99	47	73	56
Ni	68	71	49	60	56	48	40	42	43	40	44	42	32	26	32
Co	61	59	36	41	40	47	35	31	38	46	28	30	21	20	20
Sc	36	34	28	29	33	32	27	29	26	30	26	22	18	15	21
V	246	266	205	210	216	234	185	193	157	198	174	168	180	137	113
Cu	23	41	25	50	59	72	69	12	44	96	36	35	33	45	28
Pb	11	17	16	14	18	13	15	12	13	12	15	43	20	58	21
Zn	91	92	86	99	100	65	103	69	112	87	102	92	111	86	84
As	2	2	0.8	0.3	0.4	2	0.4	2	0.2	2	0.7	2	0.4	2	1
Sb	-	0.1	0.3	0.1	0.1	0.3	0.1	-	0.1	0.3	-	-	0.1	-	-
Au	0.5	0.2	2	0.4	0.3	0.6	0.3	0.1	0.3	0.7	0.2	0.4	0.2	0.1	0.3
Rb	17	19	25	22	23	20	26	24	25	27	30	32	32	40	36
Cs	0.4	0.5	2	0.4	0.5	2	0.5	0.6	0.3	2	0.2	0.8	0.4	0.3	0.6
Ba	239	210	234	142	123	151	268	166	252	170	441	362	395	427	402
Sr	649	583	686	823	665	670	824	883	713	731	708	625	602	607	669
Ta	0.2	0.2	0.3	0.2	0.2	0.3	0.3	0.3	0.4	0.2	0.3	0.4	0.5	0.4	0.4
Nb	2	2	3	3	3	3	3	3	4	3	4	4	5	5	5
Hf	2	2	2	2	2	2	2	2	3	2	2	3	3	3	3
Zr	59	63	81	76	75	75	83	79	71	74	92	85	122	94	111
Y	11	13	15	15	14	18	18	17	19	17	18	19	23	18	20
Th	1	1	2	1	1	1	2	1	1	2	2	2	2	3	3
U	1	1	2	1	1	1	1	1	—	1	2	1	1	1	1
Petrochemical parammeters															
Nb/La	0.20	0.29	0.30	0.31	0.33	0.32	0.24	0.30	0.28	0.25	0.25	0.19	0.19	0.23	0.28
Hf/Ta	8.5	9.5	7.3	9.5	11.0	7.0	7.0	8.0	6.5	9.0	8.0	6.5	6.2	7.3	7.5
La/Ta	40.5	41.50	34.67	44	44	35	42.33	37.67	33.25	59.50	55.67	56.50	49.40	49.25	46.50
Hf/Th	2.4	2.4	1.2	2.1	1.7	1.6	1.2	2.0	1.9	0.9	1.3	1.6	1.3	0.9	1.2
Th/Yb	0.70	0.67	1.23	0.69	1.13	0.86	0.94	0.71	0.76	1.14	0.94	0.86	0.94	1.32	1.27
Th/Nb	0.4	0.3	0.6	0.3	0.4	0.4	0.5	0.4	0.4	0.6	0.4	0.4	0.5	0.7	0.5
K/Rb	186	192	216	215	238	299	345	259	398	283	434	462	594	401	415
Rb/Zr	0.29	0.30	0.31	0.29	0.31	0.27	0.31	0.30	0.35	0.36	0.33	0.38	0.26	0.43	0.32
CaO/Y	0.98	0.78	0.74	0.68	0.74	0.62	0.48	0.66	0.53	0.58	0.45	0.38	0.27	0.34	0.33
Normative composition (CIPW)															
Qz	-	-	-	-	-	-	5.46	0.64	1.3	0.11	5.12	4.88	8.56	8.79	10.16
Or	4	4	4.02	3.52	4.08	2.31	6.62	4.58	7.38	5.7	9.52	10.93	14.04	11.81	11.09
Ab	11.89	12.61	14.86	13.45	16.19	21.19	20.37	19.34	20.17	20.57	26.64	29.36	33.62	32.5	30.25
An	45.72	46.56	44.87	45.9	43.34	42.09	34.61	40.49	32.54	37.42	28.19	25.21	22.97	23.9	30.04
Di	6.66	1.99	9.65	1.2	4.67	11.26	6.68	13.42	14.99	9.13	9.14	8.81	5.61	4.92	1.57
Hy	1.34	13.08	12.64	24.22	11.96	5.64	21.12	16.71	18.8	21.34	17	16.86	11.64	14.47	13
Ol	23.84	14.86	8.75	4.54	12.72	12.71	-	-	-	-	-	-	-	-	-
Mg	3.12	2.89	2.56	2.71	2.72	2.53	2.35	2.14	2.44	2.34	2.02	1.99	1.45	1.64	1.53
Il	2.77	2.71	2.14	2.46	2.56	2.03	2.15	2.28	1.94	2.33	1.71	1.42	1.34	1.26	1.62
Ap	0.55	1.14	0.39	1.8	1.58	0.16	0.54	0.29	0.34	0.94	0.56	0.45	0.68	0.63	0.66
Color index	38	36	36	35	35	34	32	35	38	35	30	29	20	22	18

— = not detected

TABLE 2. REE contents in the different rocks of the Shahira layered mafic intrusion, southern Sinai, Egypt

Sample	Chilled margin		Pyroxene-hornblende gabbro							Diorite		Quartz-diorite		
	Sh1	Sh3	Sh6	Sh11	Sh15	Sh17	Sh10	Sh18	Sh20	Sh22	Sh25	Sh31	Sh33	Sh36
La	8.1	8.3	10.4	8.8	8.8	10.5	11.3	13.3	11.9	16.7	22.6	24.7	19.7	18.6
Ce	18.6	20.1	24.8	20.6	20.8	26.0	29.8	33.9	27.6	38.5	53.8	60.5	47.9	45.2
Pr	2.56	2.81	3.53	3.03	2.90	3.66	4.09	4.69	4.13	4.91	6.49	7.01	5.86	5.09
Nd	11.1	11.5	15.6	13.0	12.1	16.5	17.9	20.9	18.2	23.1	27.1	30.2	23.8	22.3
Sm	3.09	3.33	4.04	3.28	3.24	4.18	4.77	4.96	4.42	5.53	6.03	6.94	6.56	5.5
Eu	0.90	0.92	1.07	1.08	0.97	1.12	1.31	1.38	1.18	1.33	1.42	1.75	1.65	1.23
Gd	2.39	2.61	3.01	2.82	2.60	3.13	3.71	3.92	3.39	4.56	4.31	5.81	5.568	4.7
Tb	0.40	0.45	0.51	0.44	0.43	0.52	0.61	0.64	0.55	0.68	0.64	0.86	0.82	0.7
Dy	2.37	2.59	3.17	3.01	2.72	3.30	3.76	3.79	3.52	4.15	3.96	5.29	4.74	4.19
Ho	0.45	0.49	0.58	0.58	0.52	0.63	0.72	0.76	0.69	0.81	0.77	1.06	1.01	0.85
Er	1.25	1.39	1.71	1.64	1.47	1.79	2.02	2.19	1.88	2.11	2.01	2.94	2.71	2.27
Tm	0.17	0.20	0.24	0.23	0.20	0.26	0.29	0.31	0.28	0.3	0.28	0.38	0.37	0.31
Yb	1.00	1.19	1.46	1.31	1.15	1.51	1.70	1.85	1.66	1.92	1.86	2.56	2.42	2.05
Lu	0.13	0.15	0.20	0.19	0.16	0.22	0.24	0.25	0.24	0.26	0.27	0.36	0.34	0.29
ΣREE	52.51	56.03	70.32	60.01	58.06	73.32	82.22	92.88	79.64	104.86	131.54	150.36	123.45	113.28
Eu/Eu*	1.01	0.95	0.94	1.09	1.02	0.95	0.95	0.96	0.93	0.81	0.85	0.84	0.83	0.74
$(La/Yb)_n$	5.48	4.72	4.82	4.54	5.17	4.70	4.49	4.86	4.85	5.88	8.22	6.52	5.50	6.14
$(La/Sm)_n$	1.65	1.57	1.62	1.69	1.71	1.59	1.50	1.69	1.70	1.91	2.37	2.25	1.90	2.13
$(Gd/Lu)_n$	2.25	2.13	1.84	1.82	1.99	1.74	1.89	1.92	1.73	2.15	1.96	1.98	2.01	1.99
$(La/Lu)_n$	6.38	5.67	5.33	4.75	5.64	4.89	4.82	5.45	5.08	6.58	8.58	7.03	5.94	6.57

amphibole geobarometers to the SLMI are listed in Table 3. The fine-grained gabbro (chilled margin) yielded the highest crystallization pressure between 4.5 and 6.9Kb with an average of ~ 5.9Kb, while the hornblende gabbro yielded crystallization pressure ranging from 4.5 to 6.30Kb with an average of ~5.4Kb. The dioritic rocks retrieve the lowest crystallization pressure between 1.0 and 4.4Kbar, with an average of ~2.3Kbar. The average pressures estimated for hornblende crystallization in the fine-grained gabbro and hornblende gabbro (6 and 5Kbar, respectively) indicate an intrusion depth of about 15–20km. Whereas, the average pressure (2.1Kbar) estimate for hornblende crystallization in the quartz-diorite indicate a shallower depth of emplacement (<10km). Several geothermometers were used to estimate the crystallization temperatures for the studied rocks of the SLMI. Blundy and Holland (1990) proposed a geothermometer based on coexisting amphibole-plagioclase pairs. The application of this geothermometer yields a crystallization temperature of the fine-grained gabbro between ~850° to 930ºC, the hornblende gabbro ranging from ~835° to 900ºC, whereas the quartz-diorite shows the lowest temperature of crystallization ranging from 720° to 795ºC.

Ridolfi *et al.* (2010) proposed new thermobarometric formulations to calculate the pressure, temperature and oxygen fugacity of magma. The obtained results (Table 3) using the spreadsheet provided by Ridolfi *et al.* (2010) show that the amphibole of the fine-grained gabbro formed in a relatively higher pressure (2.1–3.7kbar) than the hornblende gabbro (2.0–3.2kbar) and diorites (0.8–1.8kbar). The fine-grained gabbro (chilled margin) formed at higher temperatures (889–958ºC) than hornblende gabbro (885–934ºC) and diorites (765–862ºC). The pressure estimates obtained with the most recent calibration of Ridolfi *et al.* (2010) for amphibole are lower than those of Hollister *et al.* (1987) and Schmidt (1992). It is now well established that geobarometers that only consider Al contents in amphibole (such as Hollister *et al.*, 1987; Schmidt, 1992) tend to overestimate pressure between 0.5–4.8kb, 2.8kb on average (Bachman and Dungman, 2002; Ridolfi *et al.*, 2008).

Oxygen fugacity

The primary amphiboles of the SLMI show markedly high Fe^{3+}/Fe^{2+} ratios (0.40–1.85) and low $Fe_{(t)}/(Fe_{(t)}+Mg)$ ratios (0.31–0.38), indicating high fO_2 for the parental magma (*e.g.* Anderson and Smith, 1995; Zhang *et al.*, 2015). Moreover, in the primary amphibole $Fe_{(t)}/(Fe_{(t)}+Mg)$ *versus* Al^{IV} diagram (Anderson and Smith, 1995), the SLMI data fall in the field of high fO_2 conditions (Fig. 8). Amphibole compositions have been used to calculate fO_2 following the method of Ridolfi *et al.* (2010). The results show that log fO_2 range from -10.2 to -11.28 in gabbros and from -11.3 to -13.1 in diorites.

DISCUSSION

Neoproterozoic mafic magmatism preserved in the Sinai Peninsula constitute only a small fraction of the basement rocks, but they can provide important information about

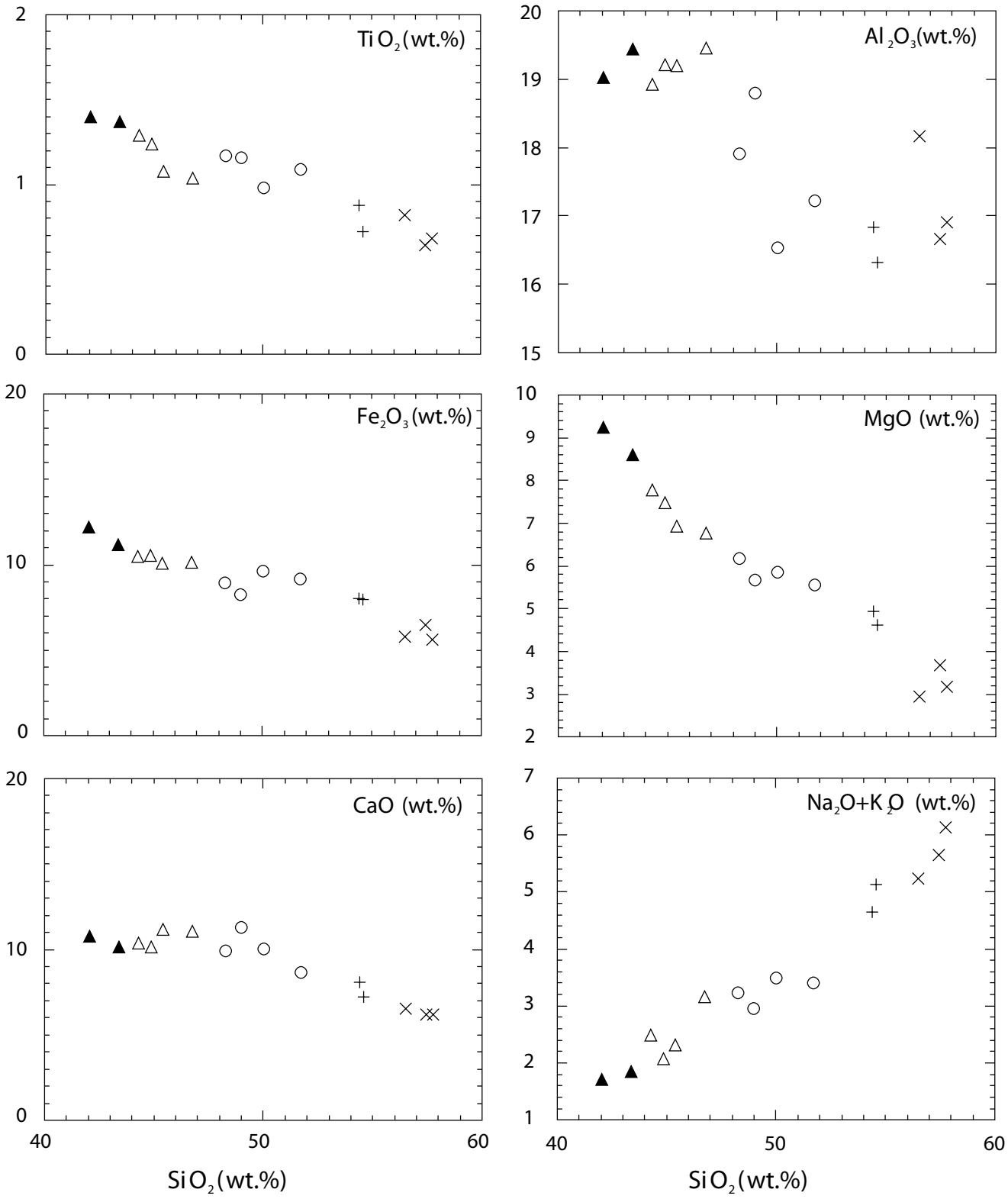

FIGURE 5. Silica variation diagrams of some major oxides for the SLMI. Symbols are as in Figure 4.

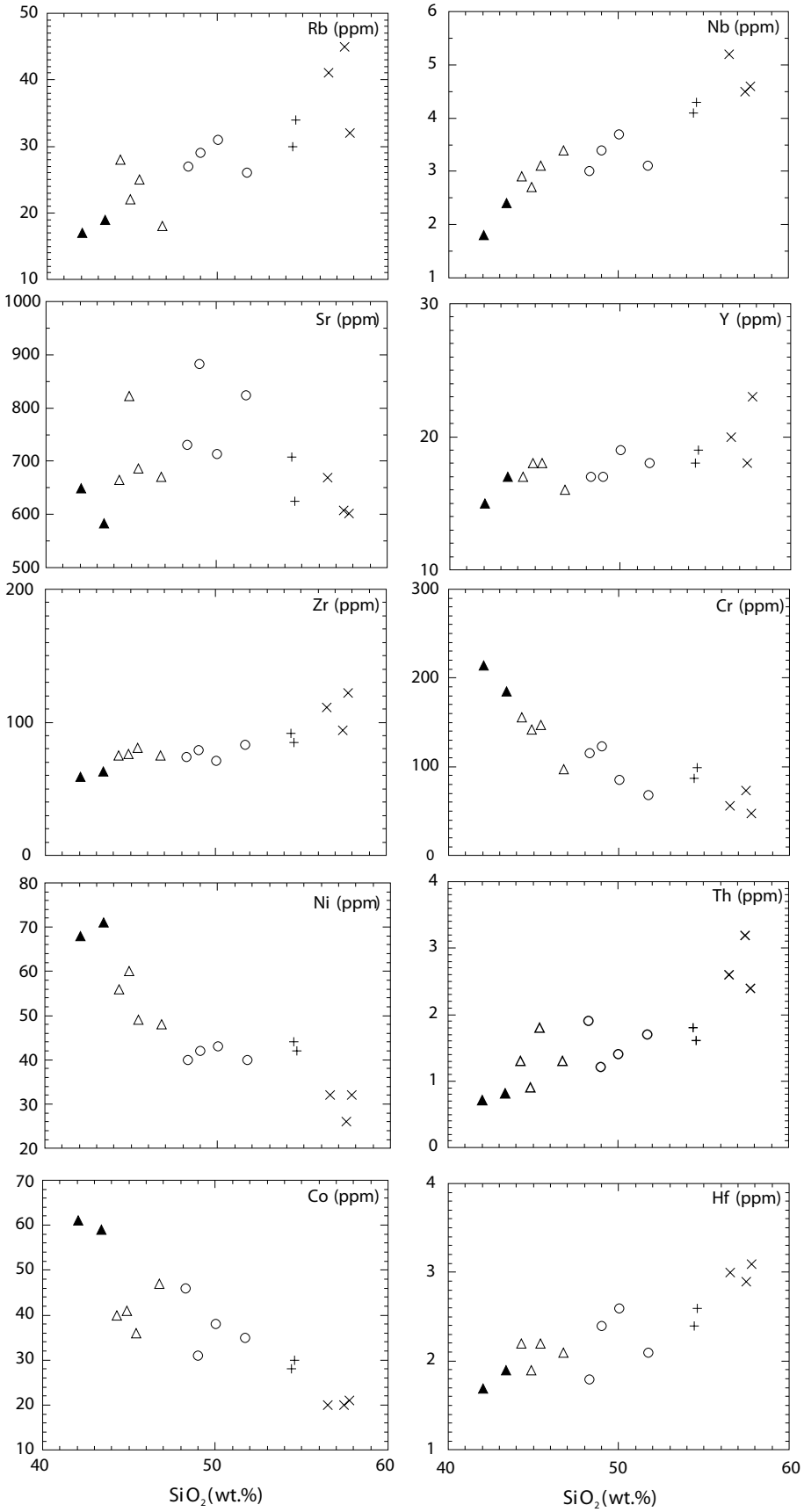

FIGURE 6. Silica variation diagrams of some trace elements for the SLMI. Symbols are as in Figure 4.

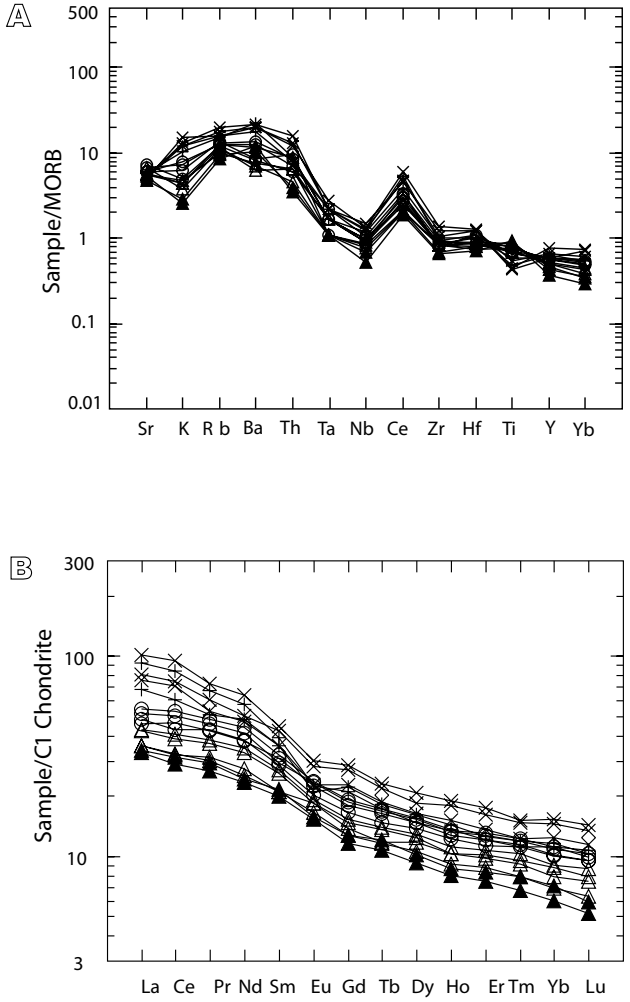

FIGURE 7. A) MORB normalized trace element plots for the samples of the SLMI with normalization values of Pearce (1983), and B) Chondrite normalized REE plots for the samples of SLMI with normalization values of Evensen *et al.* (1978). Symbols are as in Figure 4.

crustal growth processes, magma compositions and their petrogenetic evolution, nature of tectonic environments and major thermal events. The majority of felsic igneous rocks in Sinai are thought to have been derived from a variety of crustal sources and thus the mafic rocks give only indirect evidence for mantle processes (*e.g.* Abu Anbar, 2009; Azer *et al.*, 2012). Based on field, petrography, mineralogy and geochemistry of the SLMI, the following sections will assess tectonic setting, magma source and processes that thought to be responsible for generation and evolution of such layered mafic intrusions in southeast Sinai.

Nature of the parental magma

On the basis of petrographic and geochemical studies, it is clear that the SLMI rock units are co-magmatic and underwent fractional crystallization. The parental magma composition of the SLMI can be estimated via the fine-grained gabbro (chilled margin), that most probably represents rapid cooling of the original mafic melt composition. In the variation diagrams (Figs. 5; 6), the composition of the fine-grained gabbro indicate its early differentiated rock. In the Th/Ta *versus* Ta/Hf diagram (Fig. 9A), the SLMI rock units plot between the fields of Depleted MOR Mantle (DMM) and Upper Crust (UC). The fine-grained gabbro, the most primitive gabbro, plots closer than the DMM field. The plotting of the SLMI rocks between the DMM and UC suggests that the Shahira gabbros were mainly derived from partial melting of a depleted mantle source, being mixed with crustal material. Geochemical data indicate that the SLMI possesses geochemical characteristics similar to arc-related magmas (Fig. 10), like low Nb, Ta, Zr, and Y contents (Pearce, 1983). The trace element patterns of the SLMI are thought to reflect the melting of depleted mantle source relative to MORB source. In addition, the higher concentrations of LILE and LREE in the SLMI gabbroic rocks can be explained by mantle mafic magma with variable degrees of crustal contamination (Bryant *et al.*, 2006). The slightly positive εNd(T) values (+2 to +4.5) in the calc-alkaline gabbros of southern Sinai suggest their derivation from mildly depleted lithospheric mantle with some crustal component (Eyal *et al.*, 2010).

The parental magma of the SLMI does not represent primary mantle magma because its low Mg# (<64.18). The maximum Mg# values (63.82–64.18) recorded in the fine-grained gabbro suggest an early differentiation. High Wo (45.06%–48.10%) and Cr_2O_3 (0.38–0.81wt.%) content in the Clinopyroxene, and Fo (81.61%–83.29%) content in olivine, indicate that these minerals are products of hydrous mafic magmas (Sisson and Grove, 1993). In addition, the presence of anorthite-rich plagioclase (up to 70.2%, Table V) suggests an early liquid composition enriched in Al and H_2O and depleted in Na (Claeson and Meurer, 2004; Sisson and Grove, 1993). Considering all these geochemical data, it is suggested that the studied rocks of the SLMI have been derived from a hydrous high-Al mafic parental magma. The hydrous nature of the magma is supported by the common occurrence of hornblende.

The mineral chemistry of mafic minerals reflects the composition of parental magma(s) and the physical conditions of crystallization. The Al_2O_3 content in the clinopyroxene shows a marked enrichment with differentiation, as indicated by plotting of Al_2O_3 *versus* Mg# (Fig. 9B). The trend is similar to that shown by clinopyroxene of arc rocks (Loucks, 1990) and dissimilar to the trend typically observed in low-pressure anorogenic igneous provinces such as mid-ocean ridges or back-arc basins (Loney and Himmelberg, 1992; Loucks, 1990). The trend of alumina enrichment with differentiation reflects

TABLE 3. Physical-chemical conditions of the primary amphiboles of Shahira layered mafic intrusion

Rock type	Sample No.	P (kbars)		T (°C)	P (kbars)	$logfO_2$
		Hollister *et al.* (1987)	Schmidt (1992)	(Ridolfi *et al.*, 2010)		
Chilled margin	CH3	4.6	4.9	897	2.1	-11.0
		5.6	5.8	910	2.7	-11.1
		5.1	5.3	920	2.4	-11.1
		5.8	5.9	915	2.8	-11.0
		6.5	6.5	938	3.4	-10.7
		4.7	4.9	901	2.1	-10.8
		6.0	6.1	926	3.0	-11.0
		4.5	4.8	889	2.1	-11.2
		6.5	6.5	953	3.4	-10.2
		6.6	6.6	954	3.5	-10.2
		6.7	6.6	958	3.5	-10.2
		6.5	6.5	947	3.4	-10.4
		6.8	6.8	946	3.7	-10.6
		6.4	6.4	939	3.3	-10.7
Hornblende gabbro	Ch20	6.3	6.3	934	3.2	-10.7
		5.4	5.6	910	2.6	-10.9
		5.2	5.4	922	2.4	-10.9
		5.1	5.3	911	2.4	-11.3
		6.2	6.2	924	3.1	-11.1
		4.8	5.1	897	2.2	-11.3
		5.6	5.8	907	2.7	-11.2
		5.3	5.5	929	2.5	-10.8
		4.4	4.8	885	2.0	-11.1
		4.6	4.9	894	2.1	-10.9
Quartz-diorite	Ch31	1.2	2.0	779	0.9	-12.8
		1.0	1.9	765	0.8	-13.1
		1.4	2.2	777	0.9	-13.0
		4.0	4.4	862	1.8	-11.5
		1.8	2.5	799	1.0	-12.2
		3.0	3.5	830	1.4	-11.8
		3.9	4.3	862	1.7	-11.6
		2.0	2.7	797	1.1	-12.4
		1.6	2.4	796	1.0	-12.5
		1.2	2.0	798	0.9	-12.2
		1.4	2.2	796	0.9	-12.4
		1.8	2.5	835	1.0	-11.3
		1.6	2.4	817	1.0	-11.8
		1.2	2.1	777	0.9	-12.8

the crystallization of clinopyroxene from progressively more hydrous melt of arc magma (Conrad and Kay, 1984; Loucks, 1990).

In the TiO_2 *versus* Al_2O_3 discrimination diagram of amphiboles (Fig. 9C), the primary amphiboles from fine-grained gabbro and hornblende gabbro fall in the mantle source field. Whereas, those of the quartz-diorite fall in the crust-mantle mixed source. In the MgO *versus* FeO/(FeO+MgO) discrimination diagram (Zhou, 1986), all biotites of the quartz-diorite lie in the field of mixed crust-mantle source (Fig. 9D). The Fo content of olivine (<83mole%) in the fine-grained gabbro is significantly lower than that of olivine derived from a primary mantle magma (Fo> 85mole%, Fig. 3A). This, together with the low-Ni content in olivine indicates that the parental mafic magma were not directly formed by partial melting of mantle source, but may have experienced fractional crystallization before emplacement.

Fractional crystallization

Field observations indicate that the gabbros are in gradational contact with the diorites. The variation diagrams (Figs. 5; 6) show linear relationships between gabbros and diorites. These features indicate that the SLMI was evolved through fractional crystallization. This process would lead to enrichment in REE and incompatible trace elements in the diorites than the gabbros. The negative correlation between SiO_2 and MgO, Fe_2O_3, CaO, Cr, Ni and Co from gabbros to diorites indicates that ferromagnesian phases like olivine, pyroxene, amphibole and biotite were involved through subsequent fractionation crystallization process. Positive correlation between CaO and MgO (Table 1) supports the fractionation of clinopyroxene. The continuous depletion in MgO, CaO, Ni, Cr and Co from pyroxene-hornblende gabbro to diorites (Table 1) indicates that amphiboles were the dominant fractionating phase, after pyroxenes have ceased to crystallize. Low TiO_2 content in the Shahira diorites is consistent with the fractionation of Fe-Ti oxides and amphiboles. Negative correlation between MgO and Sr, from pyroxene-hornblende gabbro to hornblende gabbro, indicates that crystallization of plagioclase had an important role during fractional crystallization. As well, the CaO/Y ratio can be used as an indicator of fractional crystallization processes (Lambert and Holland, 1974). The decreasing of the CaO/Y ratio from gabbros (0.48–0.98) to diorites (0.27–0.45) implies fractionation of plagioclase and hornblende.

The present study indicates that the initial magma of the SLMI evolved after crystallization of hornblende which was caused by slight increasing of H_2O in magma after crystallization of anhydrous liquidus olivine, clinopyroxene and Ca-rich plagioclase. The crystallization of anhydrous phases in the early stages of gabbro resulted in the increase of water pressure in the remaining magma and the stabilization of calcic amphiboles in the interstitial liquid (Azer *et al.*, 2012). This is indicated by the occurrence of hornblende as oikocrysts.

Crustal contamination

Mantle-derived mafic magmas have the potential to be contaminated by crustal materials during ascent through continental crust to shallow levels (Chen *et al.*, 2008; Halama *et al.*, 2004; Hora *et al.*, 2009). The presence of few gneiss xenoliths within the margins of the Shahira gabbros suggests limited crustal contamination. In general,

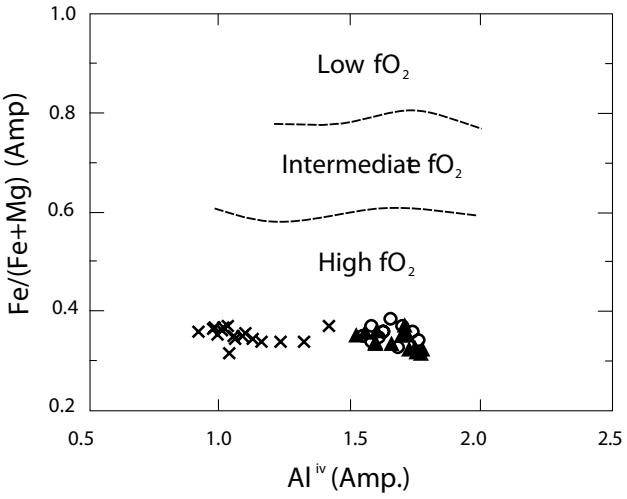

FIGURE 8. $Fe_{(t)}/(Fe_{(t)}+Mg)$ *vs.* A^{IV} diagram of the primary amphiboles (Anderson and Smith, 1995). Symbols are as in Figure 4.

the crustal component may be derived from older pre-Neoproterozoic crust (*e.g.* El-Gaby, 2007) or reworking of younger juvenile crust (*e.g.* Morag *et al.*, 2011). The geochemistry of the SLMI cannot be deciphered between the two sources. Crustal contribution to calc-alkaline mafic magmas is recorded in the north ANS (Abdel-Karim, 2013; Abu Anbar, 2009; Azer, 2007). The O and Hf isotope compositions of the SLMI are consistent with crustal contamination by Pre-ANS crustal material (Be'eri-Shlevin *et al.*, 2010).

Major and trace element geochemistry can be used to test possible contamination processes during differentiation of the magma, and to define the nature of magma source. The SLMI rocks show a wide range of K/Rb (186–594) ratio (Table 1) consistent with contamination by upper crustal rocks during evolution, particularly in the dioritic rocks. This geochemical ratio does not significantly change during fractional crystallization but change via crustal contamination (Davidson *et al.*, 1987, 1988). The crustal contribution is supported by the presence of mafic microgranular enclaves in the diorites. Moreover, it is evident that the fractional crystallization process alone cannot explain the coincidence in REE patterns of gabbro and diorite rocks (Fig. 7B), where both fractional crystallization and assimilation may have been involved. Considering all the concerned data, the mafic rocks of the SLMI were likely derived from mafic mantle magma with minor crustal contamination.

Tectonic setting

Previous studies on the SLMI created a considerable controversy on its origin and tectonic setting. This intrusion was previously related to different tectonic settings. The SLMI have been interpreted as a dismembered ophiolite (Shimron, 1981), as formed in a back-arc setting (El-Gharbawy and Hassen, 2001; Furnes *et al.*, 1985), as formed in an arc setting (Eyal *et al.*, 2014; Hassanen, 1989; Moghazi *et al.*, 1998), as formed in a post-collisional setting (Be'eri-Shlevin *et al.*, 2009; Eyal *et al.*, 2010) or as formed in a continental within-plate setting (Takla *et al.*, 2001).

Tectonic setting of the SLMI can be evaluated by using HFSE and transition elements because of the relative immobility of these elements during low grade metamorphism and hydrothermal alteration. All the SLMI rocks plot in the destructive basalts field in the Hf-Th-Nb tectonic discrimination diagram (Wood, 1980; Fig. 10A). The SLMI has Nb/La ratios of 0.2–0.3 (≤1), Hf/Ta ratios of 6.2–9.5 (>5), La/Ta ratios 33.25-59.5 (>15), Hf/Th ratios of 0.9–2.4 (<8) and Th/Yb ratios of 0.7–1.3 (>0.1). These geochemical parameters are typically of volcanic-arc basalts (Condie, 1989), and therefore we infer that these rocks were formed in a volcanic-arc setting. The volcanic-arc tectonic setting of the SLMI is substantiated by using chemistry of the mafic minerals (pyroxene and biotite). All clinopyroxene analyses of gabbroic samples plot in the subalkaline field (Fig. 3B) and in the volcanic-arc field (Fig. 10B). The biotites of the Shahira quartz-diorite have FeO*/MgO ratios (1.23 to 1.59) similar to that of calc-alkaline, subduction-related orogenic biotites (Fig. 3D).

Eyal *et al.* (2014) considered that the metamorphic complexes in southern Sinai are equivalent to three successive island arcs: the Sa'al island arc evolved from 1030 to 930Ma, the Feiran-Elat island arc from ca. 870 to 740Ma, and the Kid island arc from 640-620Ma. The Shahira gabbros provided a zircon U-Pb age of 632±4Ma (Be'eri-Shlevin *et al.*, 2009). This age is younger than the ophiolite metagabbros of the Eastern Desert of Egypt (~720-740: Ali *et al.*, 2010; Andresen *et al.*, 2009; Kröner *et al.*, 1992; Zimmer *et al.*, 1995), but comparable with Kid island arc (640–620Ma; Eyal *et al.*, 2014).

LATE NEOPROTEROZOIC MAFIC-ULTRAMAFIC INTRUSIONS OF THE ARABIAN-NUBIAN SHIELD (ANS): A COMPARISON

A comparison between the SLMI and those of the ANS may give a new perspective on how mantle-derived melts varied in time and space during the evolution of the Pan-African orogeny in the ANS. Geochemically, the SLMI is compatible with a volcanic-arc setting. In addition, the deformed nature and low grade metamorphism of the SLMI and its field relationships indicate that it pre-dates the main post-collisional stage. This is supported by the more recently zircon U-Pb age of the Shahira gabbro (632±4Ma; Be'eri-Shlevin *et al.*, 2009).

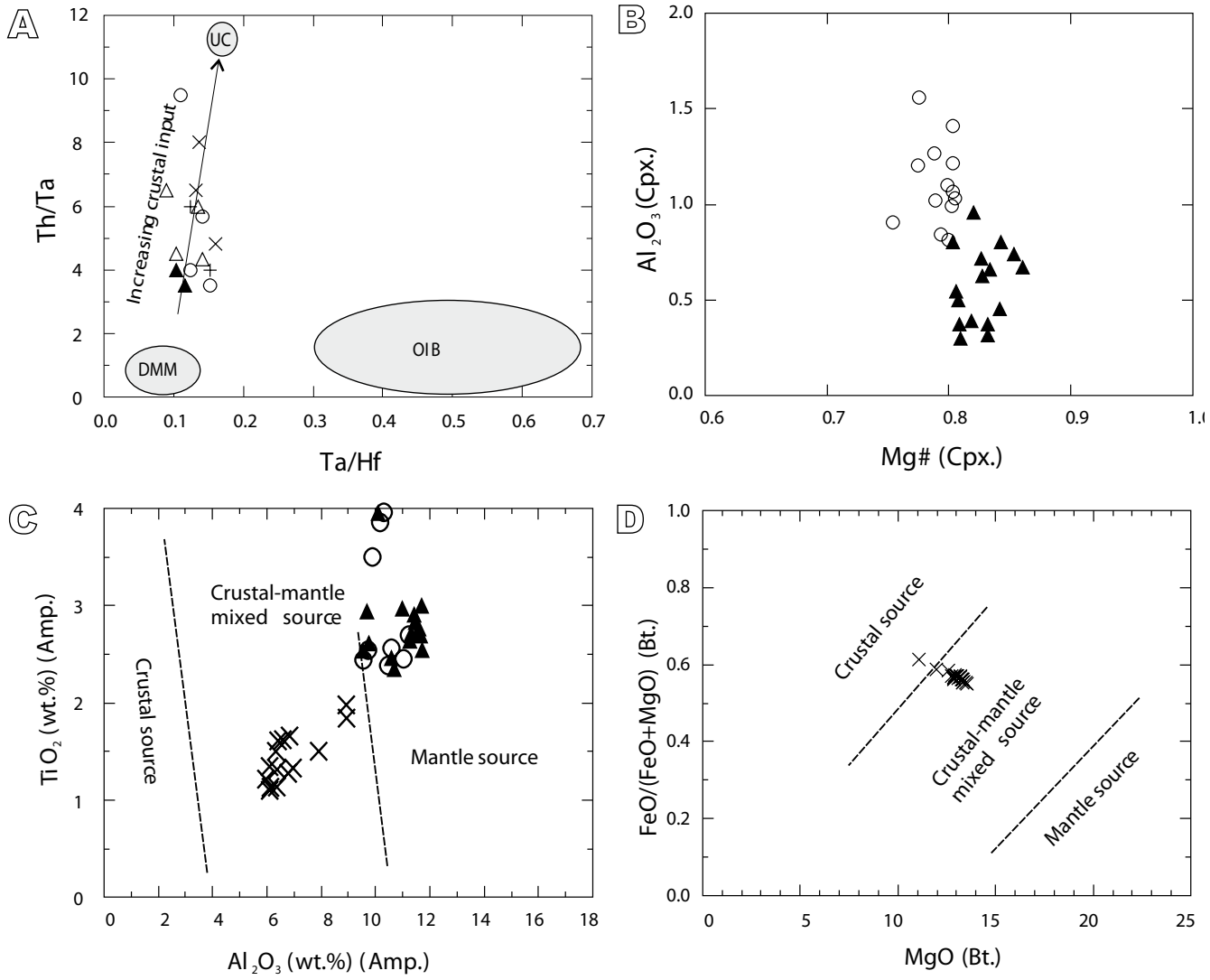

FIGURE 9. A) Ta/Hf *vs* Th/Ta diagram (Manya, 2014) for the SLMI. Depleted MOR Mantle (DMM) data is from Workman and Hart (2005), Upper Crust (UC) from Rudnick and Gao (2003) and Ocean Island Basalt (OIB) from Sun and McDonough (1989), B) Al_2O_3 *versus* Mg# for the clinopyroxenes of the Shahira layered mafic intrusion, C) plot of TiO_2 versus Al_2O_3 (after Jiang and An, 1984) for the primary amphiboles of the SLMI, D) MgO *versus* FeO/(FeO+MgO) diagram (after Zhou, 1986) for the biotites of Shahira quartz-diorite. Symbols are as in Figure 4.

According to Be'eri-Shlevin *et al.* (2009, 2011), the calc-alkaline magmatism is divided into two suites. The first suite (650–625Ma) is late/syn-orogenic and comprises a group of older deformed plutons and the associated volcanic rocks that have experienced ductile deformation. The second suite (625–590Ma) is more abundant and includes slightly deformed to mostly undeformed post-collision calc-alkaline intrusions. Field relationships, petrography, mineralogy, geochemistry and age dating of the SLMI (632±4Ma; Be'eri-Shlevin *et al.*, 2009) indicate that it is similar to the syn-orogenic calc-alkaline gabbros of southern Sinai. This is supported by the low grade metamorphism and ductile deformation in some parts of the SLMI.

The SLMI and the ultramafics of Kabr El-Bonaya (Fig. 1B) were named as Dahab mafic-ultramafics and considered to be affiliated to an ophiolite suite (Abdel Khalek *et al.*, 1994; Abu El-Enen and Makroum, 2003; Beyth *et al.*, 1978; Shimron, 1981). On the other hand, some authors have considered the ultramafic rocks of Kabr El-Bonaya part of a magmatic intrusion (Madbouly, 2000; Moussa, 2002; Takla *et al.*, 2001). Ultramafic rocks of Kabr El-Bonaya occur as two extremely small elongated masses of serpentinized peridotite and serpentinite. These two masses are totally isolated and have no connection with gabbroic rocks, but some authors thought that the SLMI was connected with Kabr El-Bonaya ultramafic rocks (El-Gaby *et al.*, 1991; Furnes *et al.*, 1985; Shimron, 1980). Based on the available data about the Kabr El-Bonaya

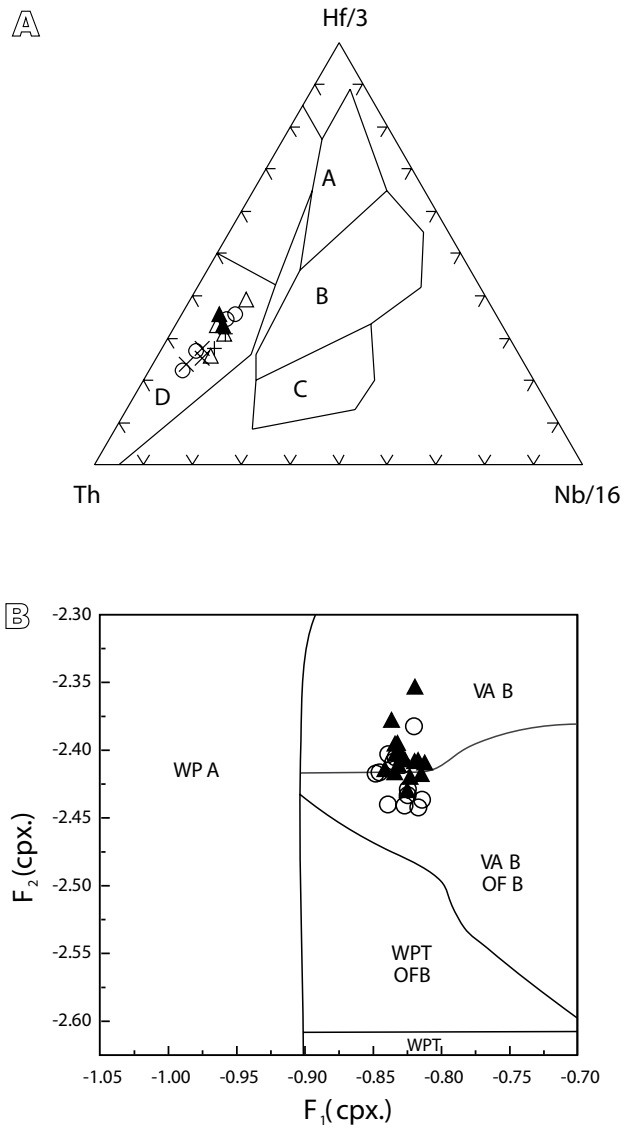

FIGURE 10. A) Hf-Th-Nb ternary diagram (Wood, 1980) for the SLMI (A: N-MORB, B: enriched MORB and within-plate tholeiites, C: within-plate basalts, and D: destructive plate basalts); and B) F1-F2 discrimination diagram of the composition of the clinopyroxenes (Nisbet and Pearce, 1977) of the SLMI (VAB: Volcanic Arc Basalt, OFB: Ocean Floor Basalt, WPT: Within-Plate Tholeiitic basalt, WPA: Within-Plate Alkali basalt). Symbols are as in Figure 4.

ultramafic rocks (Madbouly, 2000; Moussa, 2002), they are comparable with the Egyptian layered mafic intrusions of volcanic-arc setting rather than ophiolite or continental within-plate settings. Therefore, the SLMI may be connected with the Kabr El-Bonaya ultramafic rocks.

Geochemically, the Mg# of the SLMI gabbroic rocks (54.2–64.2) is lower than those of the mafic rocks of ophiolites in the Eastern Desert of Egypt (61–81, Abd El-Rahman *et al.*, 2009; Ali *et al.*, 2010), but comparable to those of the Egyptian layered mafic-ultramafic intrusions (Mg#= 58.40-68.76; Azer and El-Gharbawy, 2011; Essawy *et al.*, 1997). Moreover, the Al_2O_3/SiO_2 ratios (0.012–0.021) of the SLMI are generally similar to those of the Egyptian layered intrusions (Al_2O_3/SiO_2= 0.028–0.207, Azer and El-Gharbawy, 2011; Essawy *et al.*, 1997; Helmy and El-Mahallawi, 2003; Khudeir, 1995b).

Mineralogically, the NiO (<0.15wt.%) and Fo (<83mole%) contents of olivines of the SLMI are lower than those of the Egyptian ophiolites (Fo= 92-96, Ahmed, 2013; Gahlan *et al.*, 2015; Khalil and Azer, 2007; Khalil *et al.*, 2014; Khedr and Arai, 2013; Obeid *et al.*, 2015), but generally similar to those of the Egyptian layered mafic-ultramafic intrusions (Abd El-Rahman *et al.*, 2012; Ahmed *et al.*, 2008; Essawy *et al.*, 1997;). The olivines are characterized by low MnO (<0.24wt.%) and CaO (<0.01wt.%) contents, both of which being typical for layered mafic intrusions (Abd El-Rahman *et al.*, 2012; Ahmed *et al.*, 2008; Azer and El-Gharbawy, 2011; Essawy *et al.*, 1997).

The Mg# of orthopyroxene (0.82–0.86) and clinopyroxenes (0.75–0.86) of the SLMI are lower than those of ophiolitic rocks (Ahmed, 2013; Khedr and Arai, 2013), but similar to the Egyptian layered mafic-ultramafic intrusions (Abd El-Rahman *et al.*, 2012; Ahmed *et al.*, 2008; Azer and El-Gharbawy, 2011; Essawy *et al.*, 1997; Farahat and Helmy, 2006). The present data indicate that the field, petrographical, geochemical and mineralogical characteristics of the SLMI are akin to the Egyptian layered mafic-ultramafic intrusions of volcanic-arc setting rather than either ophiolite, post-orogenic or continental within-plate setting.

CONCLUSIONS

i) The SLMI is the earliest intrusion in the study area and exhibits a chilled margin against the older metamorphic rocks. It comprises three varieties: pyroxene-hornblende gabbros, hornblende gabbros and diorites. Field observations indicate that the gabbros are in gradational contacts with the diorites.

ii) The Rocks of the SLMI were affected by low grade regional metamorphism where calcic plagioclase is replaced by albite and epidote. Pyroxene and primary amphiboles are partly replaced by chlorite, actinolite, biotite and iron oxides.

iii) The SLMI was originated from mafic mantle-derived magma that experienced low-pressure fractional crystallization and crustal contamination producing gabbros and diorites. The formation of gabbroic rocks started with an early fractional crystallization stage which led to the

formation of a magma chamber, whereas dioritic rocks were formed in a later stage of magmatic differentiation. The parental mafic magma evolved after the crystallization of hornblende, which was caused by slight increasing of H_2O in magma after crystallization of subliquidus olivine, clinopyroxene and Ca-rich plagioclase.

iv) The gabbroic rocks of the SLMI crystallized at pressures between 4.3 and 6.8kbar (~15–20km depth).Whereas diorites yielded the lowest pressure of crystallization, from 1.0 to 4.3Kbar (<10km depth). Temperature was estimated by several geothermometers that yielded crystallization temperatures ranging from 835º to 958ºC for the gabbros and from 665º to 862ºC for the diorites.

v) The present data indicate that field, petrographical, geochemical and mineralogical characteristics of the SLMI are akin to the Egyptian layered mafic-ultramafic intrusions of volcanic-arc setting rather than the ophiolitic rocks.

ACKNOWLEDGEMENTS

This work was supported by King Saud University, Deanship of Scientific Research, Research Group No (RG-1436-036). Special thanks are given to two anonymous reviewers for their useful comments as well as to the journal editorial handling.

REFERENCES

Abd El-Rahman, Y., Polat, A., Dilek, Y., Fryer, B.J., El-Sharkawy, M., Sakran, S., 2009. Geochemistry and tectonic evolution of the Neoproterozoic incipient arc-fore-arc crust in the Fawakhir area, Central Eastern Desert of Egypt. Precambrian Research, 175(1-4), 116-134.

Abd El-Rahman, Y., Helmy, H.M., Shibata, T., Yoshikawa, M., Arai, S., Tamura, A., 2012. Mineral chemistry of the Neoproterozoic Alaskan-type Akarem Intrusion with special emphasis on amphibole: Implications for the pluton origin and evolution of subduction-related magma. Lithos, 155, 410-425.

Abdel-Karim, A.M., 2013. Petrology, geochemistry and petrogenetic aspects of Younger gabbros from south Sinai: A transition from arc to active continental margin. Chemie der Erde-Geochemistry, 73(1), 89-104.

Abdel Khalek, M.I., Abdel Maksoud, M.A., Abdel Tawab, M.A., El-Bedawi, M.A., 1994. An ophiolite-mélange complex south of Dahab, Sinai, Egypt. Annals of Geological Survey of Egypt, XX, 1-18.

Abdel-Rahman, A.M., 1994. Nature of biotites from alkaline, calcalkaline and peraluminous magmas. Journal Petrology, 35(2), 525-541.

Abu Anbar, M.M., 2009. Petrogenesis of the Nesryin gabbroic intrusion in SW Sinai, Egypt: new contributions from mineralogy, geochemistry, Nd and Sr isotopes. Mineralogy and Petrology, 95, 87-103.

Abu El-Ela, F.F., 1996. The petrology of the Abu Zawal gabbroic intrusion, Eastern Desert, Egypt: an example of an island-arc setting. Journal of African Earth Sciences, 22, 147-157.

Abu El-Ela, F.F., 1997. Geochemistry of an island-arc plutonic suite: Wadi Dabr intrusive complex, Eastern Desert, Egypt. Journal of African Earth Sciences, 24, 473-496.

Abu El-Enen, M.M., 2008. Geochemistry and metamorphism of the Pan-African back arc Malhag volcano-sedimentary Neoproterozoic association, wadi Kid area, southeast Sinai, Egypt. Journal of African Earth Science, 51(4), 189-206.

Abu El-Enen, M.M., Makroum, F.M., 2003. Tectonometamorphic evolution of the northeastern Kid Belt, Southeast Sinai, Egypt. Annals of Geological Survey of Egypt, 26, 19-37.

Abu El-Enen, M.M., Will, T.M., Okrusch, M., 2004. P-T evolution of the Pan-African Taba metamorphic belt, Sinai, Egypt: Constraints from metapelitic mineral assemblages. Journal of African Earth Sciences, 38, 59-78.

Ahmed, A.H., 2013. Highly depleted harzburgite–dunite–chromitite complexes from the Neoproterozoic ophiolite, south Eastern Desert, Egypt: A possible recycled upper mantle lithosphere. Precambrian Research, 233, 173-192.

Ahmed, A.H., Helmy, H.M., Arai, S., Yoshikawa, M., 2008. Magmatic unmixing of spinel from late Precambrian concentrically-zoned mafic-ultramafic intrusions, Eastern Desert, Egypt. Lithos, 104, 85-98.

Ali, K.A., Azer, M.K., Gahlan, H.A., Wilde, S.A., Samuel, M.D., Stern, R.J., 2010. Age constraints on the formation and emplacement of Neoproterozoioc ophiolites along the Allaqi-Heiani suture, South Eastern Desert of Egypt. Gondwana Research, 18, 583-595.

Aly, S.M., El Baraga, M.H., 1997. Geology and geochemistry of Shahira metagabbro-diorite complex, Sinai. Annals of Geological Survey of Egypt, 20, Part I, 221-233.

Anderson, J.L., Smith, D.R., 1995. The effects of temperature and fO_2 on the Al-in-hornblende barometer. American Mineralogist, 80(5-6), 549-559.

Andresen, A., Abu El-Rus, M.A., Myhre, P.I., Boghdady, G.Y., Corfu, F., 2009. U-Pb TIMS age constraints on the evolution of the Neoproterozoic Meatiq Gneiss Dome, Eastern Desert, Egypt. International Journal of Earth Sciences, 98, 481-497.

Avigad, D., Gvirtzman, Z., 2009. Late Neoproterozoic rise and fall of the northern Arabian–Nubian shield: The role of lithospheric mantle delamination and subsequent thermal subsidence. Tectonophysics, 477, 217-228.

Azer, M.K., 2007. Tectonic significance of Late Precambrian calc-alkaline and alkaline magmatism in Saint Katherina area, South Sinai, Egypt. Geologica Acta, 5(3), 255-272.

Azer, M.K., El-Gharbawy, R.I., 2011. Contribution to the Neoproterozoic layered mafic-ultramafic intrusion of Gabal Imleih, south Sinai, Egypt: Implication of post-collisional magmatism in the north Arabian-Nubian Shield. Journal of African Earth Sciences, 60, 253-272.

Azer, M.K., Stern, R.J., Kimura, J.-I., 2010. Origin of a Late Neoproterozoic (605±13 Ma) intrusive carbonate-albitite complex in Southern Sinai, Egypt. International Journal of Earth Sciences, 99, 245-267.

Azer, M.K., Abu El-Ela, F.F., Ren, M., 2012. The petrogenesis of late Neoproterozoic mafic dyke-like intrusion in south Sinai, Egypt. Journal of Asian Earth Sciences, 54-55, 91-109.

Bachmann, O., Dungan, M., 2002. Temperature-induced Al-zoning in hornblendes of the Fish Canyon magma, Colorado. American Mineralogist, 87(8-9), 1062-1076.

Basta, F.F., 1998. Mineralogy and petrology of some gabbroic intrusions in Sinai and the Eastern Desert, Egypt. Annals of Geological Survey of Egypt, 21, 239-271.

Be'eri-Shlevin, Y., Katzir, Y., Whitehouse, M., 2009. Post-collisional tectono-magmatic evolution in the northern Arabian-Nubian Shield (ANS): Time constraints from ion-probe U-Pb dating of zircon. Journal of Geological Society of London, 166(1), 71-85.

Be'eri-Shlevin, Y., Katzir, Y., Blichert-Toft, J., Kleinhanns, I.C., Whitehouse, M., 2010. Nd-Sr-Hf-O isotope provinciality in the northernmost Arabian-Nubian Shield: implications for crustal evolution. Contributions to Mineralogy and Petrology, 160, 181-201.

Be'eri-Shlevin, Y., Samuel, M.D., Azer, M.K., Rämö, O.T., Whitehouse, M.J., Moussa, H.E., 2011. The Ediacaran Ferani and Rutig volcano-sedimentary successions of the northernmost Arabian–Nubian Shield (ANS): New insights from zircon U-Pb geochronology, geochemistry and O-Nd isotope ratios. Precambrian Research, 188, 21-44.

Beyth, M., Hrunhagen, H., Zilberfarb., A., 1978. An ultramafic rock in the Precambrian of Eastern Sinai. Geological Magazine, 115(5), 373-378.

Beyth, M., Stern, R., Altherr, R., Kröner, A., 1994. The late Precambrian Timna igneous complex, Southern Israel: evidence for comagmatic-type sanukitoid monzodiorite and alkali granite magma. Lithos, 31(3), 103-124.

Bielski, M., 1982. Stages in the evolution of the Arabian-Nubian Massif in Sinai. Doctoral Thesis. Jerusalem, Hebrew University, 155pp.

Blundy, T.D., Holland, J.J.B., 1990. Calcic amphibole equilibria and a new amphibole-plagioclase geothermometer. Contribution to Mineralogy and Petrology, 104(2), 208-224.

Bogoch, R., Magaritz, M., 1983. Immiscible silicate-carbonate liquids as evidenced from ocellar diabase dykes, Southeast Sinai. Contribution to Mineralogy and Petrology, 83(3), 227-230.

Brooijmans, P., Blasband, B., White, S.H., Visser, W.J., Dirks, P., 2003. Geothermobarometric evidence for a metamorphic core complex in Sinai, Egypt. Precambrian Research, 123(2-4), 249-268.

Bryant, J.A., Yogodzinski, G.M., Hall, M.L., Lewicki, J.L., Bailey, D.G., 2006. Geochemical constraints on the origin of volcanic rocks from the Andean Northern Volcanic zone, Ecuador. Journal of petrology, 47(6), 1147-1175.

Chen, B., Tian, W., Jahn, B.M., Chen, Z.C., 2008. Zircon SHRIMP U-Pb ages and in-situ Hf isotopic analysis for the Mesozoic intrusions in South Taihang, North China craton: Evidence for hybridization between mantle-derived magmas and crustal components. Lithos, 102(1-2), 118-137.

Claeson, D.T., Meurer, W.P., 2004. Fractional crystallization of hydrous basaltic ''arc type" magmas and the formation of amphibole-bearing gabbroic cumulates. Contributions to Mineralogy and Petrology, 147(3), 288-304.

Condie, K.C., 1989. Geochemical changes in basalts and andesites across the Archean – Proterozoic boundary: identification and significance. Lithos, 23(1-2), 1-18.

Conrad, W.K., Kay, R.W., 1984. Ultramafic and mafic inclusions from Adak Island: crystallization history, and implications for the nature of primary magmas and crustal evolution in the Aleutian arc. Journal of Petrology, 25(1), 88-125.

Cox, K.G., Bell, J.D., Pankhurst, R.J., 1979. The interpretation of Igneous Rocks. London, Allen & Unwin, 450pp.

Davidson, J.P., Dungan, M.A., Ferguson, K.M., Colucci, M.T., 1987. Crust-magma interactions and the evolution of arc magmas: the San Pedro-Pellado Volcanic Complex Southern Chilean Andes. Geology, 15(5), 443-446.

Davidson, J.P., Ferguson, K.M., Colucci, M.T., Dungan, M.A., 1988. The origin of magmas from the San Pedro-Pellado Volcanic complex, S. Chile: multicomponent sources and open system evolution. Contribution to Mineralogy and Petrology, 100(4), 429-445.

Deer, W.A., Howie, R.A., Zussman, J., 1992. An introduction to the rock forming minerals. London, Longman Scientific and Technical, Second Edition, 696pp.

El-Bialy, M.Z., 2010. On the Pan-African transition of the Arabian–Nubian Shield from compression to extension: the post-collision Dokhan volcanic suite of Kid-Malhak region, Sinai, Egypt. Gondwana Research, 17(1), 26-43.

El-Gaby, S., 2007. Integrated classification and evolution of the Neoproterozoic Pan-African Belt in Egypt. The Fifth International Conference on the Geology of Africa, 1, 143-154.

El-Gaby, S., List, F.K., Tehrani, R., 1988. Geology, evolution and metallogenesis of the Pan-African belt in Egypt. In: El-Gaby, S., Greiling, R.O. (eds.). The Pan-African belt of northeast Africa and adjacent areas. Germany, Friedrich Vieweg & Sohn, 17-66.

El-Gaby, S., List, F.K., Tehrani, R., 1990. The basement complex of the Eastern Desert and Sinai. In: Said, R. (ed.). The geology of Egypt. Rotterdam, A.A. Balkema, 175-184.

El-Gaby, S., Khudeir, A.A., Abdel Tawab, M., Atalla, R.F., 1991. The metamorphosed volcano-sedimentary succession of Wadi Kid, southeastern Sinai, Egypt. Annals of Geological Survey of Egypt, 17, 19-35.

El-Gharbawy, R.I.A., Hassen, I.S., 2001. The late Precambrian metagabbro-diorite comlex, Wadi Melheg area, southeastern Sinai, Egypt: An active continental margin setting. Annals of Geological Survey of Egypt, 24, 131-158.

El-Metwally, A.A., El-Aasy, I.E., Ibrahim, M.E., Essawy, M.A., El-Mowafy, A.A., 1999. Petrological, structural and geochemical studies on the basement rocks of Gabal Um-Zariq-Wadi Kid area, South Eastern Sinai. Egyptian Journal of Geology, 43(1), 147-180.

El-Ramly, M.F., 1972. A new geological map for the basement rocks in the Eastern and Southwestern Deserts of Egypt. Annals of Geological Survey of Egypt, 2, 1-18.

El-Sayed, M.M., Furnes, H., Mohamed, F.H., 1999. Geochemical constraints on the tectonomagmatic evolution of the late Precambrian Fawakhir ophiolite, Central Eastern Desert, Egypt. Journal of African Earth Sciences, 29(3), 515-533.

El Sharkawy, M.A., El Bayoumi, R.M., 1979. The ophiolites of Wadi Ghadir area, Eastern Desert, Egypt. Annals of Geological Survey of Egypt, 9, 125-135.

Essawy, M.A., El-Metwally, A.A., Althaus, E., 1997. Pan-African layered mafic-ultramafic-mafic cumulate complex in the SW Sinai massif: mineralogy, geochemistry and crustal growth. Chemie der Erde, 57(2), 137-156.

Evensen, N.M., Hamilton, P.J., O'Nions, R.K., 1978. Rare earth abundances in chondritic meteorites. Geochimica Cosmochimica Acta, 42(8), 1199-1212.

Eyal, Y., 1980. The geological history of the Precambrian Metamorphic rocks between Wadi Twaiba and Wadi UmMara, NE Sinai. Israel Journal of Earth Sciences, 29, 53-66.

Eyal, Y., Amit, O., 1984. The Magrish Migmatites (Northeastern Sinai) and their genesis by metamorphic differentiation triggered by a change in the strain orientation. Israel Journal of Earth Sciences, 33, 188-200.

Eyal, M., Bartov, Y., Shimron, A.E., Bentor, Y.K., 1980. Sinai geological map, aeromagnetic map, 1:500.000. Survey of Israel.

Eyal, M., Litvinovsky, B., Jahn, B.M., Zanvilevich, A., Katzir, Y., 2010. Origin and evolution of post-collisional magmatism: coeval Neoproterozoic calc-alkaline and alkaline suites of the Sinai Peninsula. Chemical Geology, 269(3-4), 153-179.

Eyal, M., Be'eri-Shlevin, Y., Eyal, Y., Whitehouse, M.J., Litvinovsky, B., 2014. Three successive Proterozoic island arcs in the Northern Arabian–Nubian Shield: Evidence from SIMS U-Pb dating of zircon. Gondwana Research, 25(1), 338-351.

Farahat, E.S., Helmy, H.M., 2006. Abu Hamamid Neoproterozoic Alaskan-type complex, south Eastern Desert, Egypt. Journal of African Earth Sciences, 45, 187-197.

Furnes, H., Shimron, A.E., Roberts, D., 1985. Geochemistry of Pan-African volcanic arc sequences in SE Sinai Peninsula and plate tectonic implications. Precambrian Research, 29(4), 359-382.

Gahlan, H.A., Azer, M.K., Khalil, A.E.S., 2015. The Neoproterozoic Abu Dahr ophiolite, South Eastern Desert, Egypt: Petrological characteristics and tectonomagmatic evolution. Mineralogy and Petrology, 109(5), 611-630.

Genna, A., Nehlig, P., Le Goff, E., Guerrot, C., Shanti, M., 2002. Proterozoic tectonism of the Arabian Shield. Precambrian Research, 117, 21-40.

Ghoneim, M.F., Takla, M.A., Lebda, E., 1992. The gabbroic rocks of Central Eastern Desert, Egypt: A geochemical approach. Annals of Geological Survey of Egypt, 18, 1-21.

Halama, R., Marks, M., Brügmann, G., Siebel, W., Wenzel, T., Markl, G., 2004. Crustal contamination of mafic magmas: evidence from a petrological, geochemical and Sr-Nd-Os-O isotopic study of the Proterozoic Isortoq dike swarm, South Greenland. Lithos, 74(3-4), 199-232.

Halpern, M., Tristan, N., 1981. Geochronology of the Arabian-Nubian Shield in southern Israel and eastern Sinai. Journal of Geology, 89(5), 639-648.

Hassanen, M.A., 1989. Geochemistry and petrogenetic evolution of a late Precambrian metagabbro-diorite complex, southeast Sinai, Egypt. First Conference on the Geochemistry, Alexandria University, 118-139.

Hastie, A.R., Kerr, A.C., Pearce, J.A., Mitchell, S.F., 2007. Classification of altered volcanic island arc rocks using immobile trace elements: development of Th-Co discrimination diagrams. Journal of petrology, 48(12), 2341-2357.

Helmy, H.M., El Mahallawi, M.M., 2003. Gabbro Akarem mafic-ultramafic complex, Eastern Desert, Egypt: a Late Precambrian analogue of Alaskan-type complex. Mineralogy and Petrology, 77, 85-108.

Hollings, P., Wyman, D., 1999. Trace element and Sm-Nd systematics of volcanic and intrusive rocks from the 3 Ga Lumby Lake Greenstone belt, Superior Province: evidence for Archean plume-arc interaction. Lithos, 46(2), 189-213.

Hollister, L.S., Grissom, G.C., Peters, E.K., Stowell, H.H., Sisson, V.B., 1987. Confirmation of the empirical correlation of Al in hornblende with pressure of solidification of calc-alkaline plutons. America Mineralogist, 72, 231-239.

Hora, J.M., Singer, B.S., Wörner, G., Beard, B.L., Jicha, B.R., Johnson, C.M., 2009. Shallow and deep crustal control on differentiation of calc-alkaline and tholeiitic magma. Earth and Planetary Science Letters, 285(1-2), 75-86.

Jiang, C.Y., An, S.Y., 1984. On chemical characteristics of calcic amphiboles from igneous rocks and their petrogenesis significance (in Chinese with English abstract). Journal of Mineralogy and Petrology, 3, 1-9.

Johnson, P.R., Woldehaimanot, B., 2003. Development of the Arabian-Nubian Shield: perspectives on accretion and deformation in the northern East African Orogen and the assembly of Gondwana. In: Yoshida, M., Dasgupta, S., Windley, B. (eds.). Proterozoic East Gondwana: Supercontinent Assembly and Breakup. Geological Society of London, 206 (Special Publications), 289-325.

Khalaf, E.A., Obeid, M.A., 2013. Tectonostratigraphy and depositional history of the Neoproterozoic volcano-sedimentary sequences in Kid area, southeastern Sinai, Egypt: Implications for intra-arc to foreland basin in the northern Arabian-Nubian Shield. Journal of Asian Earth Sciences, 73(5), 473-503.

Khalil, A.E.S., Azer, M.K., 2007. Supra-subduction affinity in the Neoproterozoic serpentinites in the Eastern Desert, Egypt: Evidence from mineral composition. Journal of African Earth Sciences, 49 (4-5), 136-152.

Khalil, A.E.S., Obeid, M.A., Azer, M.K., 2014. Serpentinized peridotites at the north part of Wadi Allaqi district (Egypt): Implications for the tectono-magmatic evolution of fore-arc crust. Acta Geologica Sinica, 88(5), 1801-1840.

Khedr, M.Z., Arai, S., 2013. Origin of Neoproterozoic ophiolitic peridotites in south Eastern Desert, Egypt, constrained from primary mantle mineral chemistry. Mineralogy and Petrology, 107, 807-828.

Khudeir, A.A., 1995a. Chromian spinel-silicate chemistry in peridotite and orthopyroxenite relicts from ophiolitic serpentinites, Eastern Desert, Egypt. Assiut University, Bulletin of Faculty of Sciences, 24, 221-261.

Khudeir, A.A., 1995b. El-Genina El-Gharbia and El-Genina El-Sharkia ultramafic-mafic intrusions, Eastern Desert, Egypt: geology, petrology, geochemistry and petrogenesis. Assiut University, Bulletin of Faculty Sciences, 2-F, 177-219.

Kröner, A., Todt, W., Hussein, I.M., Mansour, M., Rashwan, A.A., 1992. Dating of late Proterozoic ophiolites in Egypt and the Sudan using the single grain zircon evaporation technique. Precambrian Research, 59, 15-32.

Kröner, A., Krüger, J., Rashwan, A.A.A., 1994. Age and tectonic setting of granitoid gneisses in the Eastern Desert of Egypt and south-west Sinai. Geologische Rundschau, 83, 502-513.

Lambert, R.St.J., Holland, J.G., 1974. Yttrium geochemistry applied to petrogenesis utilizing calcium-yttrium relationships in minerals and rocks. Geochimica Cosmochimica Acta, 38(9), 1393-1414.

Le Bas, M.J., 1962. The role of aluminum in igneous clinopyroxenes with relation to their parentage. American Journal of Sciences, 260(4), 267-288.

Leake, B.E., Woolley, A.R., Arps, C.E.S., Birch, W.D., Gilbert, M.C., Grice, J.D., Hawthorne, F.C., Kato, A., Kisch, H.J., Krivovichev, V.G., Linthout, K., Laird, J., Mandarino, J., Maresch, W.V., Nickel, E.H., Rock, N.M.S., Schumacher, J.C., Smith, D.C., Stephenson, N.C.N., Ungaretti, L., Whittaker, E.J.W., Youzhi, V., 1997. Nomenclature of amphiboles: Report of the Subcommittee on Amphiboles of the International Mineralogical Association Commission on New Minerals and Mineral Names. American Mineralogist, 82,1019-1037.

Lindsley, D.H., 1983. Pyroxene thermometry. American Mineralogist, 64, 477-93.

Loney, R.A., Himmelberg, G.R., 1992. Petrogenesis of the Pd-rich intrusion at Salt Chuck, Prince of Wales Island: an early Paleozoic Alaskan-type ultramafic body. Canadian Mineralogist, 30(4), 1005-1022.

Loucks, R.R., 1990. Discrimination of ophiolitic from nonophiolitic ultramafic-mafic allochthons in orogenic belts by the Al/Ti ratio in clinopyroxene. Geology, 18(4), 346-349.

Madbouly, M.I., 1991. Petrology and geochemistry of some mafic ultramafic rocks of Sinai, Egypt. Doctoral Thesis. Cairo University, 132pp.

Madbouly, M.I., 2000. A comparative study on petrology and geochemistry of some mafic-ultramafic intrusions of the Eastern Desert and Sinai, Egypt. Doctoral Thesis. Cairo University, 262pp.

Manya, S., 2014. Geochemistry of the Palaeoproterozoic gabbros and granodiorites of the Saza area in the Lupa Goldfield, southwestern Tanzania. Journal of African Earth Sciences, 100, 401-408.

Meert, J.G., 2003. A synopsis of events related to the assembly of eastern Gondwana. Tectonophysics, 362, 1-40.

Middlemost, E.A.K., 1997. Magmas, rocks and planetary development. Cambridge, Longman, 299pp.

Miyashiro, A., 1978. Nature of Alkalic rock series. Contribution to Mineralogy and Petrology, 66(1), 91-104.

Moghazi, A.M.,1994. Geochemical and radiogenic isotope studies of some basement rocks at the Kid area, Southeastern Sinai, Egypt. Doctoral thesis. Egypt, Alexandria University, 377pp.

Moghazi, A.M., Anderson, T., Oweiss, G.A., El Bouselly, A.M., 1998. Geochemical and Sr-Nd-Pb isotopic data bearing on the origin of Pan-African granitoids in theKid area, southeast Sinai, Egypt. Journal of the Geological Society of London, 155(4), 697-710.

Moghazi, A.M., Ali, k.A., Wilde, S.A., Zhou, Q., Andersen, T., Andresen, A., Abu El-Enen, M.M., Stern, R.J., 2012. Geochemistry, geochronology, and Sr-Nd isotopes of the Late Neoproterozoic Wadi Kid volcano-sedimentary rocks, Southern Sinai, Egypt: implications for tectonic setting and crustal evolution. Lithos, 154(1), 147-165.

Morag, N., Avigad, D., Gerdes, A., Belousova, E., Harlavan, Y., 2011. Crustal evolution and recycling in the northern Arabian-Nubian Shield: New perspectives from zircon Lu–Hf and U–Pb systematics. Precambrian Research, 186, 101-116.

Morimoto, N., Fabries, J., Ferguson, A.K., Ginzburg, I.V., Ross, M., Seifert, F.A., Zussman, J., Aoki, K., Gottardi, G., 1988. Nomenclature of pyroxenes. American Mineralogist, 73, 1123-1133.

Moussa, H.E., 2002. Mineral chemistry and geochemistry of some mafic-ultramafic intrusions in the South Eastern Desert and Sinai, Egypt. Egyptian Journal of Geology, 46, 213-238.

Nachit, H., Ibhi, A., Abia, E.H., Ohoud, M.B., 2005. Discrimination between primary magmatic biotites, reequilibrated biotites and neoformed biotites. Comptes Rendus Géoscience, 337(16), 1415-1420.

Nisbet, E.G., Pearce, J.A., 1977. Clinopyroxene composition in mafic lavas from different tectonic setting. Contribution to Mineralogy and petrology, 63, 149-160.

Obeid, M.A., Khalil, A.E.S., Azer, M.K., 2015. Mineralogy, geochemistry and geotectonic significance of the Neoproterozoic ophiolite of Wadi Arais area, south Eastern Desert, Egypt. International Geology Review, 58(6), 687-702.

Patchett, P.J., Chase, C.G., 2002. Role of transform continental margins in major crustal growth episodes. Geology, 30(1), 39-42.

Pearce, J.A., 1983. The role of sub-continental lithosphere in magma genesis at active continental margins. In: Hawkesworth, C.J., Norry, M.J. (eds.). Continental basalts and mantle xenoliths. Shiva Publisher Limi, 230-240.

Richard, L.R., 1995. Mineralogical and petrological data processing system. Minpet Software (C), 1988-1985, Version 2.02.

Ridolfi, F., Puerini, M., Renzulli, A., Menna, M., Toulkeridis, T., 2008. The magmatic feeding system of El Reventador volcano (Sub-Andean zone, Ecuador) constrained by texture, mineralogy and thermobarometry of the 2002 erupted products. Journal of Volcanology and Geothermal Research, 176(1), 94–106.

Ridolfi, F., Renzulli, A., Puerini, M., 2010. Stability and chemical equilibrium of amphibole in calc-alkaline magmas: an overview, new thermobarometric formulations and application to subduction-related volcanoes. Contribution to Mineralogy and petrology, 160(1), 45-66.

Rudnick, R.L., Gao, S., 2003. Composition of the continental crust. In: Rudnick, R.L., Holland, H.D., Turekian, K.K. (eds.). Treatise on Geochemistry. Oxford, Elsevier-Pergamon, 3, 1-64.

Schandelmeier, H., Richter, A., Harms, U., 1987. Proterozoic deformation of the East Saharan Craton in southeast Libya, south Egypt, and north Sudan. Tectonophysics, 140, 233-246.

Schmidt, M.W., 1992. Amphibole composition in tonalite as a function of pressure: an experimental calibration of the Al-in hornblende barometer. Contribution to Mineralogy and Petrology, 110, 304-310.

Shahien, M.G., 2002. Petrochemistry and petrogenesis of Kid granitoids, South Eastern Sinai, Egypt. 6th International Conference on Geology of Arab World, Cairo University, 101-118.

Shimron, A.E., 1980. Proterozoic island arc volcanism and sedimentation in Sinai. Precambrian Research, 12, 437-458.

Shimron, A.E., 1981. The Dabab mafic-ultramafic complex. A probable ophiolite of late Proterozoic (Pan-African) age. Ofioliti, 6(1), 161-164.

Shimron, A.E., 1984. Evolution of the Kid Group, southeast Sinai Peninsula: thrusts, mélanges, and implications for accretionary tectonics during the Proterozoic of the Arabian-Nubian Shield. Geology, 12(4), 242-247.

Sisson, T.W., Grove, T.L., 1993. Experimental investigations of the role of H2O in calc-alkaline differentiation and subduction zone magmatism. Contributions to Mineralogy and Petrology, 113, 143-166.

Stern, R.J., 1981. Petrogenesis and tectonic setting of late Precambrian ensimatic volcanic rocks, central Eastern desert of Egypt. Precambrian Research, 16, 195-230.

Stern, R.J., 1994. Arc assembly and continental collision in the Neoproterozoic East African Orogen: implications for the consolidation of Gondwanaland. Annual Reviews of Earth and Planetary Science, 22, 319-351.

Stern, R.J., 2002. Crustal evolution in the East African Orogen: a neodymium isotopic perspective. Journal of African Earth Sciences, 34(3), 109-117.

Stromer, J.C., 1983. The effects of recalculation on estimates of temperatures and oxygen fugacity from analyses of multicomponent iron-titanium oxides. American Mineralogist, 68, 586-594.

Stoeser, D.W., Frost, C.D., 2006. Nd, Pb, Sr and O isotope characterization of Saudi Arabian Shield terranes. Chemical Geology, 226(3-4), 163-188.

Sun, S.S., McDonough, W.F., 1989. Chemical and isotopic systematic of oceanic basalts: implication for mantle composition and processes. In: Saunders, A.D., Norry, M.J. (eds.). Magmatic in Ocean Basins. Geological Society of London, 42 (Special Publications), 313-345.

Takahashi, E., Uto, K., Schilling, J.G., 1987. Primary magma compositions and Mg/Fe ratios of their mantle residues along mid-Atlantic ridge 29N to 73N Technical Report, A9. Institute of Studies Earth's Interior, Okayama University Series, 1-14.

Takla, M.A., Basta, E.Z., Fawzi, E., 1981. Characterization of older and younger gabbros of Egypt. Delta Journal of Sciences, 5, 79-314.

Takla, M.A., Basta, F.F., Abdel Tawab, M.M., Khaled, A.M., 1991. The Precambrian rocks of Wadi Watir area, southeastren Sinai. Annals of Geological Survey of Egypt, 17, 37-52.

Takla, M.A., Basta, F.F., Madbouly, M.I., Hussein, A.A., 2001. The mafic-ultramafic intrusions of Sinai, Egypt. Annals of Geological Survey of Egypt, 24, 1-40.

Wilson, M., 1994. Igneous Petrogenesis. London, Chapman & Hall, 466pp.

Wood, D.A., 1980. The application of a Th-Hf-Ta diagram to problems of tectonomagmatic classification and to establishing the nature of crustal contamination of basaltic lavas of the British Tertiary volcanic province. Earth and Planetary Science Letters, 50(1), 11-30.

Workman, R.K., Hart, S.R., 2005. Major and trace element composition of the depleted MORB mantle (DMM). Earth Planetary Sciences and Letters, 231(1-2), 53-72.

Zhang, J.–Q., Li, S.-R., Santosh, M., Wang, J.-Z., Li, Q., 2015. Mineral chemistry of high-Mg diorites and skarn in the Han-Xing Iron deposits of South Taihang Mountains, China: Constraints on mineralization process. Ore Geology Reviews, 64, 200-214.

Zhou, Z.X., 1986. The origin of intrusive mass in Fengshandong, Hubei Province (in Chinese with English abstract). Acta Petrologica Sinica, 29(1), 59-70.

Zimmer, M., Kröner, A., Jochum, K.P., Reischmann, T., Todt, W., 1995. The Gabal Gerf complex: a Precambrian N-MORB ophiolite in the Nubian Shield, NE Africa. Chemical Geology, 123(1-4), 29-51.

Manuscript received March 2015;
revision accepted March 2016;
published Online July 2016.

ELECTRONIC APPENDIX I

TABLE I. Electron microprobe analyses of the olivines in the Shahira layered mafic intrusion

Sample No.	Sh-3							
Spot No.	Ol-14	Ol-22	Ol-32	Ol-39	Ol-51	Ol-56	Ol-67	Ol-71
Major oxides (wt.%)								
SiO_2	38.34	38.32	38.22	38.68	38.56	39.47	39.36	39.37
TiO_2	0.00	0.03	0.00	0.03	0.01	0.00	0.00	0.01
Al_2O_3	0.01	0.03	0.11	0.01	0.01	0.00	0.00	0.00
Cr_2O_3	0.06	0.14	0.06	0.08	0.07	0.33	0.06	0.23
FeO	17.36	15.83	17.32	16.55	16.45	16.52	15.86	16.90
MnO	0.20	0.22	0.24	0.18	0.16	0.19	0.24	0.24
MgO	43.69	44.87	43.77	44.05	44.24	43.29	44.31	43.28
NiO	0.14	0.08	0.06	0.15	0.14	0.09	0.03	0.07
CaO	0.01	0.01	0.00	0.01	0.01	0.01	0.00	0.00
Na_2O	0.00	0.02	0.00	0.01	0.01	0.02	0.01	0.02
K_2O	0.00	0.00	0.00	0.01	0.00	0.00	0.00	0.00
P_2O_5	0.00	0.00	0.00	0.00	0.00	0.03	0.00	0.00
Total	99.77	99.51	99.78	99.70	99.60	99.89	99.87	100.11
Structural formulae								
Si	0.98	0.97	0.98	0.98	0.98	1	0.99	1
Ti	0	0	0	0	0	0	0	0
Al	0	0	0	0	0	0	0	0
Cr	0	0	0	0	0	0	0	0
$Fe^{(ii)}$	0.37	0.34	0.37	0.35	0.35	0.35	0.34	0.36
Mn	0	0	0.01	0	0	0	0.01	0.01
Mg	1.66	1.70	1.67	1.67	1.68	1.63	1.67	1.63
Ni	0	0	0	0	0	0	0	0
Ca	0	0	0	0	0	0	0	0
End members								
Fo	81.61	83.29	81.63	82.43	82.61	82.21	83.07	81.82
Fa	18.18	16.48	18.11	17.37	17.23	17.59	16.68	17.92
Tp	0.21	0.23	0.26	0.19	0.17	0.20	0.26	0.26

TABLE II. Microprobe analyses of the biotites in the quartz-diorite of Shahira layered mafic intrusion

Rock type	Chilled margin															
Sample No.	Sh3															
Mineral	Clinopyroxene															
Spot No.	Cpx-7	Cpx-9	Cpx-16	Cpx-22/	Cpx-25	Cpx-28	Cpx-33	Cpx-36	Cpx-42	Cpx-45	Cpx-52	Cpx-53	Cpx-61	Cpx-67	Cpx-73	Cpx-79
Major oxides (wt.%)																
SiO_2	53.04	53.02	52.97	53.19	52.82	53.52	53.11	52.97	52.75	52.43	53.55	53.11	52.23	52.89	53.24	53.52
TiO_2	0.00	0.00	0.00	0.00	0.10	0.00	0.01	0.00	0.04	0.16	0.00	0.00	0.03	0.06	0.00	0.00
Al_2O_3	0.30	0.45	0.32	0.55	0.63	0.39	0.80	0.72	0.80	0.74	0.37	0.66	0.67	0.96	0.50	0.37
Cr_2O_3	0.54	0.48	0.44	0.79	0.65	0.81	0.62	0.49	0.71	0.50	0.62	0.61	0.49	0.75	0.50	0.51
FeO	7.71	7.30	7.45	7.41	7.87	7.49	7.02	7.20	6.86	7.55	7.72	7.22	7.63	7.75	7.52	7.45
MnO	0.26	0.30	0.29	0.23	0.24	0.21	0.22	0.25	0.28	0.18	0.25	0.22	0.13	0.26	0.28	0.23
MgO	14.93	14.85	14.60	15.10	14.98	14.87	14.88	14.57	14.84	14.82	15.09	15.20	14.96	14.63	14.87	14.81
CaO	22.54	23.80	23.90	22.49	22.92	23.61	23.83	23.65	22.39	23.83	22.99	22.93	23.62	23.30	22.97	24.18
Na_2O	0.29	0.25	0.24	0.25	0.30	0.25	0.28	0.29	0.26	0.25	0.23	0.31	0.23	0.31	0.25	0.23
K_2O	0.02	0.00	0.00	0.00	0.00	0.00	0.00	0.00	0.00	0.00	0.00	0.00	0.00	0.00	0.00	0.00
P_2O_5	0.00	0.00	0.00	0.00	0.04	0.03	0.02	0.01	0.00	0.00	0.00	0.00	0.01	0.00	0.00	0.00
Total	99.63	100.44	100.20	100.02	100.54	101.16	100.77	100.15	98.93	100.45	100.81	100.24	100.00	100.90	100.13	101.31
Structural formulae																
TSi	1.97	1.96	1.96	1.97	1.94	1.96	1.95	1.96	1.98	1.94	1.97	1.96	1.93	1.95	1.97	1.96
TAl	0.01	0.02	0.01	0.02	0.04	0.02	0.04	0.03	0.03	0.03	0.02	0.03	0.04	0.04	0.02	0.02
TFe^{3+}	0.01	0.02	0.03	0.01	0.02	0.02	0.01	0.01	0	0.03	0.01	0.012	0.03	0.01	0.01	0.02
M1Al	0	0	0	0	0	0	0	0	0.01	0	0	0	0	0	0	0
M1Ti	0	0	0	0	0	0	0	0	0	0	0	0	0	0	0	0
$M1Fe^{3+}$	0.03	0.05	0.04	0.02	0.06	0.03	0.05	0.05	0.01	0.06	0.03	0.04	0.07	0.05	0.03	0.04
$M1Fe^{2+}$	0.12	0.12	0.14	0.12	0.10	0.13	0.12	0.14	0.13	0.11	0.13	0.10	0.09	0.12	0.13	0.14
M1Cr	0.02	0.01	0.01	0.02	0.02	0.02	0.02	0.01	0.02	0.02	0.02	0.02	0.01	0.02	0.02	0.02
M1Mg	0.83	0.82	0.81	0.83	0.82	0.81	0.82	0.80	0.83	0.82	0.83	0.84	0.82	0.80	0.82	0.81
$M2Fe^{2+}$	0.07	0.03	0.03	0.08	0.07	0.05	0.04	0.03	0.07	0.03	0.07	0.07	0.04	0.05	0.06	0.03
M2Mn	0.01	0.01	0.01	0.01	0.01	0.01	0.01	0.01	0.01	0.01	0.07	0.01	0.00	0.01	0.01	0.01
M2Ca	0.90	0.94	0.95	0.89	0.90	0.93	0.94	0.94	0.90	0.94	0.07	0.91	0.94	0.92	0.91	0.95
M2Na	0.02	0.02	0.02	0.02	0.02	0.02	0.02	0.02	0.02	0.02	0.07	0.02	0.02	0.02	0.02	0.02
End members (%)																
WO	45.49	47.23	47.55	45.47	45.76	46.93	47.48	47.56	46.06	47.21	45.79	45.96	46.77	46.69	46.17	47.62
EN	41.94	40.99	40.43	42.47	41.61	41.14	41.26	40.76	42.46	40.84	41.81	42.39	41.23	40.78	41.59	40.58
FS	12.57	11.78	12.02	12.06	12.64	11.94	11.26	11.69	11.48	11.95	12.40	11.65	12.00	12.53	12.24	11.81
Mg#	0.81	0.84	0.83	0.81	0.83	0.82	0.84	0.83	0.80	0.85	0.81	0.83	0.86	0.82	0.81	0.83

TABLE II. Continued

Rock type	Hornblende gabbro												
Sample No.	Sh20												
Mineral	Clinopyroxene												
Spot No.	Cpx-2	Cpx-5	Cpx-17	Cpx-22	Cpx-27	Cpx-30	Cpx-33	Cpx-42	Cpx-48	Cpx-52	Cpx-58	Cpx-64	Cpx-65
Major oxides (wt.%)													
SiO_2	53.36	53.24	52.68	53.05	53.05	52.50	53.53	52.51	52.90	52.35	53.49	53.30	52.86
TiO_2	0.00	0.01	0.12	0.10	0.12	0.12	0.00	0.00	0.12	0.16	0.00	0.12	0.11
Al_2O_3	1.10	1.21	1.27	0.99	1.03	1.21	1.41	0.81	1.02	1.56	0.91	0.84	1.06
Cr_2O_3	0.53	0.66	0.63	0.66	0.60	0.58	0.46	0.50	0.58	0.55	0.64	0.75	0.38
FeO	7.38	8.30	8.28	7.57	7.76	8.51	7.03	8.10	8.28	8.33	8.36	7.70	7.55
MnO	0.23	0.22	0.19	0.24	0.21	0.24	0.21	0.20	0.27	0.23	0.20	0.29	0.17
MgO	14.73	14.66	14.11	14.84	14.26	14.07	14.78	14.29	13.86	13.97	14.42	14.52	14.38
CaO	22.90	22.18	23.29	22.64	23.81	23.74	23.06	22.95	24.05	22.76	21.98	23.32	23.19
Na_2O	0.30	0.27	0.25	0.28	0.28	0.22	0.31	0.29	0.21	0.27	0.27	0.22	0.33
K_2O	0.00	0.02	0.00	0.00	0.00	0.00	0.00	0.00	0.00	0.00	0.00	0.00	0.00
P_2O_5	0.00	0.00	0.00	0.00	0.00	0.00	0.00	0.00	0.00	0.00	0.00	0.00	0.02
Total	100.53	100.75	100.82	100.38	101.12	101.19	100.79	99.64	101.27	100.18	100.27	101.07	100.05
Structural formulae													
TSi	1.97	1.96	1.95	1.96	1.95	1.93	1.99	1.96	1.95	1.95	1.99	1.96	1.96
TAl	0.03	0.04	0.06	0.04	0.05	0.05	0.01	0.04	0.04	0.05	0.02	0.04	0.04
TFe^{3+}	0	0	0	0	0.01	0.01	0	0.01	0.01	0	0	0	0
M1Al	0.02	0.02	0	0	0	0	0	0	0	0.01	0.03	0	0.01
M1Ti	0	0	0	0	0	0	0	0	0	0	0	0	0
$M1Fe^{3+}$	0.02	0.02	0.05	0.03	0.05	0.06	0.02	0.05	0.04	0.04	0.00	0.03	0.04
$M1Fe^{2+}$	0.14	0.14	0.15	0.13	0.15	0.15	0.15	0.14	0.18	0.16	0.16	0.15	0.15
M1Cr	0.02	0.02	0.02	0.02	0.02	0.02	0.01	0.02	0.02	0.02	0.02	0.02	0.01
M1Mg	0.81	0.81	0.78	0.82	0.78	0.77	0.82	0.79	0.76	0.77	0.80	0.80	0.80
$M2Fe^{2+}$	0.07	0.10	0.06	0.08	0.04	0.04	0.05	0.06	0.03	0.07	0.10	0.06	0.05
M2Mn	0.01	0.01	0.01	0.01	0.01	0.01	0.01	0.01	0.01	0.01	0.01	0.01	0.01
M2Ca	0.90	0.88	0.92	0.90	0.94	0.94	0.92	0.92	0.95	0.91	0.87	0.92	0.92
M2Na	0.02	0.02	0.02	0.02	0.02	0.02	0.02	0.02	0.02	0.02	0.02	0.02	0.02
End members (%)													
WO	46.41	45.06	47.02	45.84	47.74	47.35	46.79	46.54	48.10	46.57	45.11	46.86	47.11
EN	41.54	41.44	39.63	41.81	39.77	39.03	41.73	40.32	38.56	39.76	41.17	40.61	40.65
FS	12.05	13.50	13.35	12.35	12.49	13.62	11.47	13.14	13.34	13.67	13.72	12.53	12.24
Mg#	0.80	0.77	0.79	0.80	0.81	0.80	0.80	0.80	0.79	0.78	0.75	0.79	0.80

TABLE II. Continued

Rock type	Chilled margin																	
Sample	Sh-3																	
Mineral	Orthopyroxene																	
Spot No.	Opx-1	Opx-8	Opx-15	Opx-19	Opx-23	Opx-26	Opx-29	Opx-31	Opx-34	Opx-38	Opx-41	Opx-47	Opx-48	Opx-50	Opx-54	Opx-66	Opx-68	Opx-70
Major oxides (wt.%)																		
SiO_2	53.98	54.55	54.41	54.34	54.20	54.10	54.34	53.92	55.00	54.42	53.93	53.63	53.56	53.74	53.66	54.58	54.35	54.29
TiO_2	0.23	0.32	0.23	0.22	1.98	0.33	0.22	0.24	0.16	0.26	0.22	0.27	0.29	0.25	0.23	0.19	0.29	0.28
Al_2O_3	2.80	2.28	2.14	2.48	2.33	2.62	2.80	3.02	1.82	2.19	2.84	2.82	2.71	2.96	2.75	3.34	2.55	2.61
Cr_2O_3	0.56	0.55	0.40	0.33	0.40	0.51	0.46	0.20	0.16	0.40	0.46	0.69	0.58	0.56	0.59	0.16	0.44	0.45
FeO	11.06	11.49	11.83	11.21	11.37	11.20	10.91	11.13	11.31	11.76	10.94	11.09	11.28	11.17	10.86	9.25	11.53	11.13
MnO	0.27	0.24	0.28	0.23	0.25	0.24	0.23	0.27	0.19	0.28	0.24	0.27	0.26	0.28	0.28	0.05	0.26	0.24
MgO	30.43	30.37	30.64	30.81	30.86	30.30	30.27	30.70	30.66	30.57	30.43	30.51	30.64	30.63	30.73	31.79	30.59	30.35
CaO	1.75	1.30	0.89	0.64	0.75	1.74	1.86	1.43	0.51	0.61	1.40	1.44	1.35	1.30	1.17	1.20	0.96	1.43
Na_2O	0.01	0.06	0.01	0.00	0.01	0.03	0.03	0.02	0.00	0.00	0.01	0.01	0.01	0.01	0.01	0.01	0.00	0.02
K_2O	0.00	0.02	0.00	0.00	0.00	0.00	0.00	0.00	0.00	0.00	0.00	0.00	0.00	0.00	0.00	0.00	0.01	0.00
P_2O_5	0.01	0.02	0.00	0.00	0.00	0.01	0.02	0.01	0.00	0.01	0.00	0.00	0.00	0.00	0.00	0.00	0.00	0.02
Total	100.63	101.18	100.83	100.25	100.36	101.07	101.16	100.93	99.81	100.51	100.46	100.72	100.68	100.89	100.27	100.56	100.96	100.93
Structural formulae																		
TSi	1.88	1.91	1.91	1.91	1.88	1.89	1.90	1.88	1.94	1.91	1.89	1.88	1.88	1.88	1.88	1.89	1.9	1.90
TAl	0.12	0.09	0.09	0.09	0.10	0.11	0.11	0.12	0.06	0.09	0.11	0.12	0.11	0.12	0.11	0.11	0.10	0.10
M1Al	0	0	0	0.01	0	0	0.01	0	0.02	0	0.01	0	0	0	0	0.03	0.01	0.01
M1Ti	0.01	0.01	0.01	0.01	0.05	0.01	0.01	0.01	0.00	0.01	0.01	0.01	0.01	0.01	0.01	0.01	0.01	0.01
M1Cr	0.02	0.02	0.01	0.01	0.01	0.01	0.01	0.01	0.00	0.01	0.01	0.02	0.02	0.02	0.02	0.00	0.01	0.01
M1Mg	0.98	0.98	0.98	0.97	0.94	0.98	0.97	0.98	0.97	0.98	0.97	0.97	0.98	0.98	0.98	0.96	0.98	0.97
M2Mg	0.61	0.61	0.62	0.64	0.66	0.60	0.60	0.61	0.64	0.62	0.62	0.62	0.62	0.62	0.63	0.69	0.62	0.61
M2Fe^{2+}	0.32	0.34	0.35	0.33	0.33	0.33	0.32	0.33	0.33	0.35	0.32	0.33	0.33	0.33	0.32	0.27	0.34	0.33
M2Mn	0.01	0.01	0.01	0.01	0.01	0.01	0.01	0.01	0.01	0.01	0.01	0.01	0.01	0.01	0.01	0.00	0.01	0.01
M2Ca	0.07	0.05	0.03	0.02	0.03	0.07	0.07	0.05	0.02	0.02	0.05	0.05	0.05	0.05	0.04	0.05	0.04	0.05
M2Na	0	0	0	0	0	0	0	0	0	0	0	0	0	0	0	0	0	0
M2K	0	0.001	0	0	0	0	0	0	0	0	0	0	0	0	0	0	0	0
End members (%)																		
WO	3.31	2.46	1.68	1.22	1.43	3.29	3.54	2.70	0.98	1.17	2.66	2.73	2.54	2.46	2.22	2.28	1.82	2.72
EN	79.99	80.17	80.48	81.75	81.38	79.80	79.96	80.52	81.81	80.94	80.71	80.47	80.45	80.64	81.26	83.95	80.74	80.38
FS	16.70	17.37	17.84	17.04	17.19	16.91	16.51	16.78	17.22	17.89	16.63	16.81	17.01	16.91	16.52	13.78	17.45	16.90

TABLE III. Microprobe analyses of the biotites in the quartz-diorite of Shahira layered mafic intrusion

Sample No.	Sh31																				
Spot No.	Bio2	Bio4	Bio11	Bio17	Bio22	Bio24	Bio27	Bio33	Bio36	Bio38	Bio43	Bio47	Bio52	Bio55	Bio57	Bio61	Bio66	Bio67	Bio69	Bio70	Bio72
Major oxides (wt.%)																					
SiO_2	36.44	36.43	35.82	37.61	37.09	35.92	35.97	36.08	36.02	36.81	35.96	35.90	35.99	35.98	36.44	35.98	36.63	36.23	36.31	36.25	37.71
TiO_2	3.38	3.62	3.58	3.32	2.48	3.42	3.51	3.45	3.42	2.76	3.91	3.72	3.81	3.90	3.38	3.83	3.38	3.80	3.67	3.67	2.75
Al_2O_3	13.67	13.99	13.87	14.39	14.30	13.64	13.89	13.62	13.56	14.24	13.90	13.75	13.75	13.80	13.93	13.76	13.90	13.99	13.81	13.90	14.59
Cr_2O_3	0.24	0.24	0.11	0.23	0.23	0.05	0.09	0.18	0.17	0.16	0.13	0.14	0.06	0.16	0.25	0.15	0.31	0.16	0.24	0.15	0.10
FeO	17.00	17.50	17.14	17.09	17.39	17.19	16.80	17.24	17.09	17.72	16.99	16.51	16.68	17.11	16.67	16.86	16.50	16.70	17.32	16.79	17.65
MnO	0.30	0.30	0.29	0.28	0.18	0.29	0.21	0.22	0.24	0.22	0.24	0.22	0.21	0.32	0.22	0.27	0.29	0.27	0.30	0.28	0.25
MgO	13.08	13.20	13.31	11.98	12.92	13.03	13.51	13.21	13.34	12.61	13.28	13.30	13.39	12.95	13.56	12.75	12.86	12.88	13.03	12.88	11.08
CaO	0.05	0.11	0.09	0.06	0.07	0.09	0.12	0.12	0.10	0.08	0.08	0.11	0.12	0.11	0.10	0.17	0.07	0.10	0.04	0.10	0.03
Na_2O	0.12	0.13	0.12	0.08	0.08	0.12	0.11	0.10	0.10	0.09	0.10	0.11	0.11	0.12	0.11	0.13	0.10	0.13	0.11	0.14	0.04
K_2O	9.45	9.31	9.32	9.66	9.37	9.33	9.39	9.34	9.39	9.27	9.45	9.03	9.04	9.27	9.27	9.26	9.03	8.92	9.66	8.89	9.51
F	0.18	0.13	0.13	0.27	0.23	0.15	0.09	0.05	0.06	0.25	0.17	0.12	0.11	0.10	0.11	0.10	0.11	0.16	0.16	0.14	0.41
Cl	0.07	0.06	0.08	0.06	0.05	0.07	0.06	0.07	0.07	0.05	0.08	0.07	0.07	0.05	0.06	0.06	0.05	0.05	0.07	0.06	0.06
P_2O_5	0.00	0.00	0.00	0.02	0.02	0.00	0.75	0.01	0.01	0.00	0.01	0.01	0.01	0.00	0.01	0.00	0.00	0.00	0.00	0.00	0.00
SO_2	0.05	0.07	0.04	0.06	0.06	0.06	0.01	0.06	0.03	0.07	0.07	0.05	0.04	0.05	0.05	0.03	0.05	0.05	0.06	0.00	0.00
Total	94.00	95.08	93.88	95.09	94.45	93.35	94.52	93.74	93.58	94.33	94.35	93.01	93.39	93.91	94.16	93.36	93.28	93.44	94.77	93.24	94.16
Structural formulae																					
Si	5.87	5.81	5.79	5.98	5.94	5.84	5.74	5.83	5.83	5.91	5.78	5.82	5.82	5.81	5.84	5.83	5.91	5.85	5.82	5.87	6.06
Al^{IV}	2.13	2.19	2.21	2.03	2.06	2.16	2.26	2.17	2.17	2.09	2.22	2.18	2.18	2.20	2.16	2.17	2.09	2.15	2.18	2.14	1.94
Al^{VI}	0.47	0.44	0.43	0.67	0.63	0.45	0.35	0.43	0.42	0.61	0.41	0.45	0.44	0.43	0.47	0.46	0.55	0.51	0.43	0.51	0.82
Ti	0.41	0.43	0.44	0.40	0.30	0.42	0.42	0.42	0.42	0.33	0.47	0.45	0.46	0.47	0.41	0.47	0.41	0.46	0.44	0.45	0.33
Fe2	2.29	2.33	2.32	2.27	2.33	2.34	2.24	2.33	2.32	2.38	2.28	2.24	2.26	2.31	2.23	2.29	2.23	2.25	2.32	2.27	2.37
Cr	0.03	0.03	0.01	0.03	0.03	0.01	0.01	0.02	0.02	0.02	0.02	0.02	0.01	0.02	0.03	0.02	0.04	0.02	0.03	0.02	0.01
Mn	0.04	0.04	0.04	0.04	0.02	0.04	0.03	0.03	0.03	0.03	0.03	0.03	0.03	0.04	0.03	0.04	0.04	0.04	0.04	0.04	0.03
Mg	3.14	3.14	3.21	2.84	3.08	3.16	3.21	3.18	3.22	3.02	3.18	3.22	3.23	3.12	3.24	3.08	3.09	3.10	3.12	3.11	2.66
Ca	0.01	0.02	0.02	0.01	0.01	0.02	0.02	0.02	0.02	0.01	0.01	0.02	0.02	0.02	0.02	0.03	0.01	0.02	0.01	0.02	0.01
Na	0.04	0.04	0.04	0.02	0.03	0.04	0.03	0.03	0.03	0.03	0.03	0.03	0.04	0.04	0.04	0.04	0.03	0.04	0.03	0.04	0.01
K	1.94	1.90	1.92	1.96	1.91	1.94	1.91	1.93	1.94	1.90	1.94	1.87	1.87	1.91	1.90	1.92	1.86	1.84	1.98	1.84	1.95
Petrochemical parammeters																					
FeO/MgO	1.30	1.33	1.29	1.43	1.35	1.32	1.24	1.31	1.28	1.41	1.28	1.24	1.25	1.32	1.23	1.32	1.28	1.30	1.33	1.30	1.59
Fe/(Fe+Mg)	0.42	0.43	0.42	0.44	0.43	0.43	0.41	0.42	0.42	0.44	0.42	0.41	0.41	0.43	0.41	0.43	0.42	0.42	0.43	0.42	0.47
Mg/(Mg+Fe)	0.58	0.57	0.58	0.56	0.57	0.57	0.59	0.58	0.58	0.56	0.58	0.59	0.59	0.57	0.59	0.57	0.58	0.58	0.57	0.58	0.53

TABLE IV. Electron microprobe analyses of the amphiboles in the Shahira layered mafic intrusion

Rock type	Fine-grained gabbro-Chilled margin																						
Sample No.	Sh3																						
Mineral	Primary amphiboles															Secondary amphiboles							
	Magnesio-hornblende				Magnesio-hastingsite			Tschermakitic hornblende								Magnesio-hornblende				Tremolite-actinolite			
Spot No.	am66	am68	am70	am75	am52	am57	am61	am13	am16	am2	am23	am25	am35	am41	am44	am20	am32	am37	am4	am55	am65	am73	am78
Major oxides (wt.%)																							
SiO_2	42.57	42.31	42.11	42.50	42.50	42.44	42.45	43.67	43.40	44.29	43.17	42.57	44.12	42.74	44.30	48.52	49.31	49.18	49.48	53.50	52.13	53.60	53.42
TiO_2	2.84	2.55	2.69	2.65	2.88	2.81	2.98	2.46	3.95	2.93	2.34	2.75	2.61	2.97	2.53	0.90	0.77	0.19	0.73	0.91	0.07	0.81	0.09
$Al2O_3$	11.49	11.77	11.35	11.29	11.52	11.61	11.72	10.60	10.12	9.72	10.71	11.42	9.78	11.02	9.57	5.71	4.62	6.53	5.09	2.52	2.52	1.62	2.08
FeO	11.49	12.37	11.61	12.42	11.63	11.36	11.22	12.73	12.19	12.80	12.91	12.63	12.66	13.34	13.09	13.67	14.37	11.69	14.04	10.44	12.39	11.65	3.96
MnO	0.01	0.01	0.04	0.04	0.03	0.01	0.01	0.09	0.06	0.13	0.07	0.08	0.07	0.16	0.07	0.45	0.49	0.24	0.18	0.26	0.00	0.07	0.08
MgO	13.65	12.84	13.61	13.02	13.89	13.81	13.86	12.99	13.67	14.18	12.96	12.90	14.31	12.76	13.70	13.78	14.76	15.13	14.80	17.51	15.40	16.49	21.93
CaO	11.54	11.60	11.38	11.61	11.59	11.60	11.65	11.65	11.18	11.08	11.47	11.47	11.16	11.19	11.26	11.07	11.10	13.59	12.00	12.62	11.76	12.08	11.19
Na_2O	1.96	1.88	2.02	1.92	2.06	2.09	2.07	1.65	2.07	1.95	1.81	1.94	2.05	1.91	1.83	1.14	0.90	0.27	0.75	0.28	0.24	0.14	0.74
K_2O	0.64	0.64	0.61	0.65	0.59	0.58	0.59	0.63	0.64	0.64	0.68	0.64	0.64	0.68	0.64	0.43	0.37	0.08	0.38	0.09	0.00	0.03	0.04
P_2O_5	0.00	0.00	0.00	0.00	0.00	0.00	0.00	0.00	0.00	0.00	0.00	0.00	0.00	0.00	0.02	0.00	0.00	0.03	0.00	0.04	0.00	0.00	0.10
Total	96.18	95.97	95.42	96.09	96.69	96.30	96.55	96.47	97.28	97.72	96.12	96.39	97.40	96.76	97.00	95.66	96.68	96.93	97.46	98.16	94.51	96.50	93.63
Structural formulae																							
TSi	6.274	6.28	6.254	6.306	6.229	6.247	6.232	6.445	6.346	6.405	6.398	6.292	6.403	6.295	6.478	7.145	7.141	7.14	7.149	7.543	7.66	7.699	7.548
TAl	1.726	1.72	1.746	1.694	1.771	1.753	1.768	1.555	1.654	1.595	1.602	1.708	1.597	1.705	1.522	0.855	0.788	0.86	0.851	0.418	0.34	0.274	0.346
TFe_3	0	0	0	0	0	0	0	0	0	0	0	0	0	0	0	0	0.071	0	0	0.039	0	0.027	0.106
Sum_T	8	8	8	8	8	8	8	8	8	8	8	8	8	8	8	8	8	8	8	8	8	8	8
CAl	0.269	0.337	0.239	0.278	0.218	0.259	0.259	0.287	0.088	0.06	0.267	0.28	0.074	0.206	0.126	0.135	0	0.256	0.015	0	0.096	0	0
CFe3	0.502	0.461	0.587	0.458	0.581	0.508	0.486	0.448	0.489	0.799	0.522	0.506	0.788	0.636	0.673	0.62	0.925	0.244	0.683	0.359	0.457	0.363	0.362
CTi	0.315	0.285	0.301	0.296	0.318	0.311	0.329	0.273	0.434	0.319	0.261	0.306	0.285	0.329	0.278	0.1	0.084	0.021	0.079	0.097	0.008	0.088	0.01
CMg	2.999	2.841	3.013	2.88	3.035	3.03	3.033	2.858	2.98	3.057	2.863	2.843	3.096	2.802	2.986	3.025	3.187	3.274	3.188	3.68	3.373	3.531	4.619
CFe_2	0.914	1.074	0.855	1.083	0.844	0.89	0.891	1.123	1.002	0.749	1.078	1.055	0.749	1.007	0.927	1.063	0.744	1.175	1.014	0.833	1.066	1.01	0
CMn	0.001	0.001	0.005	0.005	0.004	0.001	0.001	0.011	0.007	0.016	0.009	0.01	0.009	0.02	0.009	0.056	0.06	0.03	0.022	0.031	0	0.009	0.01
Sum_C	5	5	5	5	5	5	5	5	5	5	5	5	5	5	5	5	5	5	5	5	5	5	5
BCa	1.822	1.845	1.811	1.846	1.82	1.829	1.833	1.842	1.751	1.717	1.821	1.817	1.735	1.766	1.764	1.747	1.722	2	1.858	1.906	1.851	1.859	1.694
BNa	0.178	0.155	0.189	0.154	0.18	0.171	0.167	0.158	0.249	0.283	0.179	0.183	0.265	0.234	0.236	0.253	0.253	0	0.142	0.077	0.068	0.039	0.203
Sum_B	2	2	2	2	2	2	2	2	2	2	2	2	2	2	2	2	1.975	2	2	1.983	1.92	1.898	1.897
ACa	0	0	0	0	0	0	0	0	0	0	0	0	0	0	0	0	0	0.114	0	0	0	0	0
ANa	0.382	0.386	0.393	0.398	0.406	0.426	0.422	0.314	0.338	0.264	0.341	0.373	0.312	0.311	0.283	0.072	0	0.076	0.068	0	0	0	0
AK	0.12	0.121	0.116	0.123	0.11	0.109	0.111	0.119	0.119	0.118	0.129	0.121	0.118	0.128	0.119	0.081	0.068	0.015	0.07	0.016	0	0.005	0.007
Sum_A	0.503	0.507	0.508	0.521	0.516	0.535	0.532	0.433	0.458	0.382	0.47	0.493	0.431	0.439	0.402	0.153	0.068	0.205	0.138	0.016	0	0.005	0.007
Petrochemical parammeters																							
$Fe_{(t)}/(Fe_{(t)}+Mg)$	0.321	0.351	0.324	0.349	0.32	0.316	0.312	0.355	0.333	0.336	0.359	0.354	0.332	0.37	0.349	0.357	0.344	0.302	0.347	0.245	0.311	0.28	0.073
Fe^{3+}/Fe^{2+}	0.549	0.429	0.687	0.423	0.688	0.571	0.545	0.399	0.488	1.067	0.484	0.48	1.052	0.632	0.726	0.583	1.243	0.208	0.674	0.431	0.429	0.359	

TABLE IV. Continued

Rock type	Hornblende gabbro																	
Sample No.	Sh20																	
Mineral	Primary amphiboles										Secondary amphiboles							
	Tschermakite-tschermakitic hornblende										Magnesio-hornblende					Tremolite-actinolite		
Spot No.	am19	am26	am29	am31	am38	am53	am59	am68	am71	am1	am8	am15	am23	am29	am34	am47	am66	am69
Major oxides (wt.%)																		
SiO_2	43,55	43,39	43,17	42,62	43,84	43,51	42,63	44,53	44,53	42,39	50	48,31	48,36	49,59	48,32	42,62	54,61	50,56
TiO_2	2,38	3,96	3,85	2,44	3,5	2,55	4,03	2,44	2,53	2,7	0,15	0,66	0,99	0,14	0,99	2,44	0,03	0,09
Al_2O_3	10,47	10,3	10,18	11,04	9,88	10,59	10,35	9,55	9,73	11,23	6,32	5,54	5,6	6,11	6,51	11,04	1,04	3,81
FeO	13,22	11,94	13,62	13,7	12,87	13,31	12,57	13,4	12,95	12,92	12,06	14,51	14,74	12,44	12,69	13,7	3,8	13,33
MnO	0,13	0,09	0,09	0,07	0,06	0,12	0,06	0,1	0,09	0,1	0,24	0,43	0,36	0,25	0,06	0,07	0,08	0
MgO	13,37	13,85	13,06	12,28	13,54	12,7	13,65	13,94	14,3	13	15,14	14,43	13,4	15,15	14,4	12,28	22,38	14,52
CaO	11,38	11,05	10,75	11,57	10,68	11,47	10,95	11,06	11,16	11,27	12,44	11,02	11,2	13,02	12,13	11,57	12,3	11,31
Na_2O	1,78	2,03	2,07	1,82	1,9	1,71	2,02	1,9	1,95	1,9	0,71	1,23	1,36	0,69	0,97	1,82	0,7	0,52
K_2O	0,71	0,64	0,62	0,66	0,65	0,63	0,61	0,61	0,62	0,65	0,19	0,46	0,54	0,21	0,46	0,66	0,05	0,03
P_2O_5	0	0	0	0	0	0	0	0	0	0	0,02	0	0,03	0,03	0	0	0,08	0
Total	96,98	97,26	97,41	96,19	96,94	96,59	96,86	97,54	97,86	96,16	97,28	96,57	96,59	97,63	96,53	96,19	95,07	94,17
Structural formulae																		
TSi	6,378	6,323	6,306	6,348	6,396	6,423	6,244	6,455	6,424	6,268	7,189	7,03	7,119	7,156	7,069	6,348	7,678	7,477
TAl	1,622	1,677	1,694	1,652	1,604	1,577	1,756	1,545	1,576	1,732	0,811	0,949	0,881	0,844	0,931	1,652	0,172	0,523
Sum_T	8	8	8	8	8	8	8	8	8	8	8	8	8	8	8	8	8	8
CAl	0,184	0,091	0,058	0,285	0,093	0,264	0,029	0,085	0,077	0,224	0,259	0	0,09	0,194	0,191	0,285	0	0,14
CFe3	0,705	0,575	0,723	0,477	0,745	0,511	0,716	0,846	0,841	0,669	0,454	0,957	0,549	0,362	0,359	0,477	0,297	0,624
CTi	0,262	0,434	0,423	0,273	0,384	0,283	0,444	0,266	0,275	0,3	0,016	0,072	0,11	0,015	0,109	0,273	0,003	0,01
CMg	2,919	3,009	2,844	2,727	2,945	2,795	2,98	3,012	3,075	2,866	3,245	3,13	2,941	3,259	3,141	2,727	4,691	3,201
CFe2	0,914	0,88	0,941	1,23	0,825	1,133	0,824	0,778	0,721	0,929	0,996	0,787	1,266	1,139	1,194	1,23	0	1,025
CMn	0,016	0,011	0,011	0,009	0,007	0,015	0,007	0,012	0,011	0,013	0,029	0,053	0,045	0,031	0,007	0,009	0,01	0
Sum_C	5	5	5	5	5	5	5	5	5	5	5	5	5	5	5	5	5	5
BCa	1,786	1,725	1,683	1,846	1,669	1,814	1,718	1,718	1,725	1,786	1,916	1,718	1,767	2	1,901	1,846	1,853	1,792
BNa	0,214	0,275	0,317	0,154	0,331	0,186	0,282	0,282	0,275	0,214	0,084	0,282	0,233	0	0,099	0,154	0,147	0,149
Sum_B	2	2	2	2	2	2	2	2	2	2	2	2	2	2	2	2	2	1,941
ACa	0	0	0	0	0	0	0	0	0	0	0	0	0	0,013	0	0	0	0
ANa	0,291	0,299	0,269	0,372	0,207	0,304	0,292	0,252	0,27	0,33	0,114	0,065	0,155	0,193	0,176	0,372	0,044	0
AK	0,133	0,119	0,116	0,125	0,121	0,119	0,114	0,113	0,114	0,123	0,035	0,085	0,101	0,039	0,086	0,125	0,009	0,006
Sum_A	0,424	0,418	0,384	0,497	0,328	0,422	0,406	0,365	0,384	0,453	0,149	0,15	0,256	0,245	0,262	0,497	0,053	0,006
Petrochemical parammeters																		
$Fe_{(t)}/(Fe_{(t)}+Mg)$	0,36	0,33	0,37	0,38	0,35	0,37	0,34	0,35	0,34	0,36	0,31	0,36	0,38	0,32	0,33	0,38	0,06	0,34
Fe^{3+}/Fe^{2+}	0,77	0,65	0,77	0,39	0,90	0,45	0,87	1,09	1,17	0,72	0,46	1,22	0,43	0,32	0,30	0,39		0,61

TABLE IV. Continued

Rock type	Quartz-diorite																							
Sample No.	Sh31																							
Mineral	Primary amphiboles																	Secondary amphiboles						
	Magnesio-hornblende																	Magnesio-hornblende				Tremolite-actinolite		
Spot No.	am5	am8	am17	am19	am21	am25	am30	am32	am37	am42	am48	am54	am65	am66	am72	am73	am77	am4	am11	am17	am28	am41	am48	am56
Major oxides (wt.%)																								
SiO_2	47,77	45,22	47,63	46	45,02	47,22	46,93	46,94	46,94	47,43	46,57	46,7	47,42	47,44	47,57	47,31	47,86	48,55	49,73	47,82	49,53	52,18	53,45	52,89
TiO_2	1,3	1,83	1,27	1,48	1,96	1,32	1,6	1,32	1,47	1,11	1,65	1,6	1,12	1,11	1,28	1,41	1,2	1,02	0,64	0,97	0,89	0,08	0,96	0,05
Al_2O_3	6,36	8,91	6,74	7,88	8,88	6,93	6,56	6,1	6,31	6,07	6,81	6,57	6,33	6,15	6	6,48	5,93	5,5	4,86	5,87	4,99	2,7	2,42	1,71
FeO	14,34	12,55	12,37	13,02	14,19	13,26	13,82	14,04	13,79	14,17	14,25	14,06	13,94	14,49	13,6	13,35	14,35	14,63	14,84	14,2	15,03	12,26	10,55	4,13
MnO	0,38	0,1	0,05	0,16	0,15	0,08	0,47	0,39	0,31	0,36	0,32	0,42	0,42	0,47	0,45	0,34	0,43	0,34	0,42	0,45	0,43	0	0,23	0,11
MgO	13,67	13,69	14,79	14,09	13,42	14,07	13,85	14,18	14,21	13,89	14,56	14,32	13,47	13,77	13,46	13,64	13,81	13,53	15,38	13,75	15,34	15,27	17,29	21,93
CaO	10,96	11,49	11,5	11,3	11,31	11,36	11,22	11,06	11,04	11,14	10,96	11,11	10,99	11,11	11,12	11,12	10,76	11,02	10,88	11,09	10,67	11,45	12,7	11,94
Na_2O	1,32	1,57	1,16	1,34	1,69	1,05	1,19	1,36	1,41	1,34	1,2	1,11	1,22	1,17	1,25	1,33	1,25	1,32	1,06	1,24	1,16	0,31	0,74	0,6
K_2O	0,45	0,59	0,47	0,53	0,64	0,51	0,52	0,43	0,48	0,52	0,5	0,42	0,52	0,49	0,4	0,51	0,42	0,51	0,35	0,43	0,41	0,02	0,16	0,04
P_2O_5	0,03	0,02	0	0	0	0	0	0,02	0,02	0,03	0	0,03	0,02	0	0	0	0,03	0,04	0,03	0,03	0,02	0	0,04	0,14
Total	96,59	95,97	95,96	95,71	97,26	95,8	96,15	95,84	95,98	96,07	96,82	96,32	95,44	96,2	95,13	95,48	96,04	96,47	98,2	95,84	98,47	94,26	98,55	93,55
Structural formulae																								
TSi	6,983	6,674	6,96	6,763	6,579	6,936	6,897	6,909	6,899	6,985	6,747	6,813	7,02	6,964	7,074	7,006	7,015	7,133	7,055	7,047	7,008	7,67	7,568	7,541
TAl	1,017	1,326	1,04	1,237	1,421	1,064	1,103	1,057	1,092	1,015	1,162	1,129	0,98	1,036	0,926	0,994	0,985	0,867	0,812	0,953	0,831	0,33	0,404	0,287
TFe3	0	0	0	0	0	0	0	0,034	0,009	0	0,091	0,058	0	0	0	0	0	0	0,132	0	0,16	0	0,029	0,172
Sum_T	8	8	8	8	8	8	8	8	8	8	8	8	8	8	8	8	8	8	8	8	8	8	8	8
CAl	0,078	0,223	0,12	0,127	0,108	0,135	0,032	0	0	0,038	0	0	0,124	0,027	0,125	0,136	0,038	0,084	0	0,066	0	0,138	0	0
CFe3	0,762	0,502	0,622	0,741	0,742	0,668	0,748	0,842	0,808	0,736	1,061	0,97	0,672	0,845	0,535	0,537	0,87	0,617	1,145	0,735	1,175	0,475	0,142	0,32
CTi	0,143	0,203	0,14	0,164	0,215	0,146	0,177	0,146	0,163	0,123	0,18	0,176	0,125	0,123	0,143	0,157	0,132	0,113	0,068	0,108	0,095	0,009	0,102	0,005
CMg	2,979	3,012	3,222	3,088	2,924	3,081	3,034	3,111	3,113	3,049	3,145	3,115	2,973	3,013	2,984	3,011	3,017	2,963	3,253	3,021	3,236	3,346	3,65	4,661
CFe2	0,991	1,047	0,889	0,86	0,993	0,961	0,951	0,852	0,878	1,009	0,575	0,688	1,054	0,934	1,156	1,116	0,889	1,181	0,483	1,015	0,443	1,032	1,078	0
CMn	0,047	0,013	0,006	0,02	0,019	0,01	0,059	0,049	0,039	0,045	0,039	0,052	0,053	0,058	0,057	0,043	0,053	0,042	0,05	0,056	0,052	0	0,028	0,013
Sum_C	5	5	5	5	5	5	5	5	5	5	5	5	5	5	5	5	5	5	5	5	5	5	5	5
BCa	1,717	1,817	1,801	1,78	1,771	1,788	1,767	1,744	1,738	1,758	1,701	1,737	1,743	1,747	1,772	1,764	1,69	1,735	1,654	1,751	1,618	1,803	1,927	1,824
BNa	0,283	0,183	0,199	0,22	0,229	0,212	0,233	0,256	0,262	0,242	0,299	0,263	0,257	0,253	0,228	0,236	0,31	0,265	0,292	0,249	0,318	0,088	0,073	0,166
Sum_B	2	2	2	2	2	2	2	2	2	2	2	2	2	2	2	2	2	2	1,945	2	1,936	1,892	2	1,99
ANa	0,091	0,266	0,129	0,162	0,25	0,087	0,106	0,132	0,14	0,14	0,039	0,051	0,093	0,08	0,132	0,146	0,045	0,111	0	0,105	0	0	0,13	0
AK	0,084	0,111	0,088	0,099	0,119	0,096	0,097	0,081	0,09	0,098	0,092	0,078	0,098	0,092	0,076	0,096	0,079	0,096	0,063	0,081	0,074	0,004	0,029	0,007
Sum_A	0,175	0,377	0,217	0,261	0,369	0,182	0,203	0,213	0,23	0,238	0,131	0,129	0,192	0,172	0,208	0,243	0,123	0,206	0,063	0,186	0,074	0,004	0,159	0,007
Petrochemical parammeters																								
$Fe_{(t)}/(Fe_{(t)}+Mg)$	0,37	0,34	0,32	0,34	0,37	0,35	0,36	0,35	0,35	0,36	0,34	0,35	0,37	0,37	0,36	0,35	0,37	0,38	0,33	0,37	0,33	0,31	0,25	0,06
Fe^{3+}/Fe^{2+}	0,77	0,48	0,70	0,86	0,75	0,70	0,79	0,99	0,92	0,73	1,85	1,41	0,64	0,90	0,46	0,48	0,98	0,52	2,37	0,72	2,65	0,46	0,13	

TABLE V. Electron microprobe analyses of the feldspars in the Shahira layered mafic intrusion

Rock type	Chilled margin																			
Sample No.	Sh3																			
Mineral	Plagioclase																			
Spot No.	Pl-3	Pl-5	Pl-7/	Pl-10	Pl-12	Pl-17	Pl-24	Pl-27	Pl-30	Pl-37	Pl-39	Pl-40	Pl-43	Pl-46	Pl-49	Pl-55	Pl-58	Pl-60	Pl-63	Pl-71
Major oxides (wt.%)																				
SiO_2	50.40	50.69	52.18	68.52	52.34	54.21	53.45	52.44	55.77	67.14	51.02	50.13	51.10	49.86	56.33	69.12	53.41	52.19	50.33	54.80
TiO_2	0.00	0.00	0.00	0.02	0.00	0.00	0.00	0.00	0.00	0.01	0.00	0.00	0.00	0.00	0.10	0.03	0.00	0.00	0.00	0.00
Al_2O_3	31.41	31.45	30.70	19.08	30.21	29.18	29.04	30.13	27.71	20.06	31.11	31.10	31.14	31.68	26.44	18.75	29.23	30.59	31.39	28.38
FeO	0.05	0.03	0.13	0.17	0.00	0.17	0.00	0.12	0.00	0.19	0.04	0.06	0.18	0.04	0.25	0.14	0.06	0.29	0.05	0.02
MnO	0.00	0.00	0.00	0.04	0.00	0.00	0.00	0.00	0.00	0.05	0.00	0.00	0.00	0.00	0.03	0.02	0.00	0.00	0.00	0.00
MgO	0.00	0.02	0.00	0.07	0.00	0.00	0.00	0.11	0.00	0.11	0.00	0.00	0.00	0.00	0.00	0.09	0.00	0.00	0.00	0.00
CaO	14.34	13.90	12.76	1.43	12.36	11.20	11.55	12.26	9.61	1.24	13.83	14.40	13.75	14.27	8.89	0.21	11.57	12.75	13.74	10.92
Na_2O	3.44	3.66	4.25	9.61	4.36	5.10	4.87	4.28	5.98	10.35	3.85	3.47	3.72	3.30	6.47	10.45	4.84	4.26	3.62	5.55
K_2O	0.07	0.06	0.07	0.04	0.09	0.15	0.13	0.16	0.18	0.08	0.06	0.08	0.08	0.06	0.24	0.04	0.17	0.12	0.07	0.13
Total	99.71	99.81	100.09	98.97	99.36	100.03	99.04	99.50	99.25	99.22	99.90	99.25	99.98	99.22	98.76	98.85	99.27	100.18	99.20	99.81
Structural formulae																				
Si	9.21	9.24	9.46	12.05	9.54	9.79	9.75	9.55	10.10	11.84	9.29	9.21	13.48	9.15	10.26	12.15	9.72	9.46	9.23	9.91
Al	6.76	6.75	6.55	3.95	6.48	6.21	6.24	6.46	5.91	4.16	6.67	6.73	0.10	6.85	5.67	3.88	6.27	6.53	6.78	6.04
Ti	0	0	0	0	0	0	0	0	0	0	0	0	0	0	0.01	0	0	0	0	0
Fe_{+2}	0.01	0	0.02	0.03	0	0.03	0	0.02	0	0.03	0.01	0.01	0.04	0.01	0.04	0.02	0.01	0.04	0.01	0
Mn	0	0	0	0.01	0	0	0	0	0	0.01	0	0	0	0	0.01	0	0	0	0	0
Mg	0	0	0	0.02	0	0	0	0.03	0	0.03	0	0	0	0	0	0.02	0	0	0	0
Ca	2.81	2.72	2.48	0.27	2.41	2.17	2.26	2.39	1.86	0.23	2.70	2.84	3.89	2.81	1.73	0.04	2.26	2.48	2.70	2.12
Na	1.22	1.29	1.49	3.28	1.54	1.79	1.72	1.51	2.10	3.54	1.36	1.24	1.91	1.18	2.29	3.56	1.71	1.50	1.29	1.95
K	0.02	0.02	0.02	0.01	0.02	0.04	0.03	0.04	0.04	0.02	0.01	0.02	0.03	0.02	0.06	0.01	0.04	0.03	0.02	0.03
End members																				
Ab	30.1	32.2	37.4	92.2	38.7	44.8	42.9	38.4	52.4	93.4	33.4	30.2	32.7	29.4	56.1	98.7	42.6	37.4	32.2	47.6
An	69.5	67.5	62.2	7.6	60.7	54.4	56.3	60.7	46.5	6.2	66.3	69.3	66.8	70.2	42.5	1.1	56.4	61.9	67.4	51.7
Or	0.4	0.4	0.4	0.3	0.5	0.9	0.7	1	1	0.4	0.3	0.5	0.5	0.4	1.4	0.2	1	0.7	0.4	0.7

TABLE V. Continued

Rock type	Hornblende gabbro																				
Sample No.	Sh20																				
Mineral	Plagioclase																				
Spot No.	Pl-3	Pl-6	Pl-7	Pl-9	Pl-10	Pl-14	Pl-18	Pl-20	Pl-24	Pl-28	Pl-32	Pl-35	Pl-37	Pl-41	Pl-44	Pl-46	Pl-49	Pl-50	Pl-53	Pl-60	Pl-67
Major oxides (wt.%)																					
SiO_2	53.14	57.53	57.47	67.09	52.47	50.96	53.01	66.62	52.14	58.56	57.88	58.77	58.15	68.37	57.49	53.34	53.21	58.06	67.20	59.13	59.04
TiO_2	0.00	0.00	0.00	0.01	0.00	0.00	0.00	0.01	0.00	0.00	0.01	0.00	0.00	0.03	0.11	0.00	0.00	0.00	0.00	0.00	0.00
Al_2O_3	29.51	26.71	26.78	20.08	29.60	30.59	29.49	19.60	29.68	26.08	25.71	25.60	25.37	18.80	25.67	29.57	29.75	26.07	20.07	26.26	26.16
FeO	0.01	0.00	0.00	0.17	0.01	0.03	0.20	0.26	0.00	0.07	0.11	0.06	0.00	0.17	0.22	0.02	0.02	0.00	0.18	0.00	0.00
MnO	0.00	0.00	0.00	0.05	0.00	0.00	0.00	0.05	0.00	0.00	0.00	0.00	0.00	0.02	0.01	0.00	0.00	0.00	0.06	0.00	0.00
MgO	0.00	0.00	0.00	0.03	0.00	0.00	0.00	0.21	0.00	0.00	0.00	0.00	0.03	0.09	0.00	0.02	0.00	0.00	0.01	0.00	0.00
CaO	11.74	8.21	8.46	1.62	12.30	13.69	11.94	1.50	12.74	7.70	7.48	7.32	8.43	0.95	7.96	11.40	11.96	7.97	1.54	7.32	7.47
Na_2O	4.76	6.45	6.37	10.03	4.65	3.91	4.69	10.40	4.35	7.05	7.15	7.24	6.93	9.79	6.91	4.79	4.66	7.01	10.35	7.08	6.90
K_2O	0.21	0.23	0.12	0.07	0.12	0.06	0.11	0.09	0.12	0.40	0.43	0.42	0.21	0.03	0.33	0.11	0.17	0.24	0.09	0.29	0.14
Total	99.37	99.13	99.19	99.15	99.15	99.24	99.44	98.73	99.03	99.85	98.77	99.42	99.11	98.24	98.71	99.26	99.76	99.35	99.50	100.08	99.71
Structural formulae																					
Si	9.67	10.37	10.36	11.83	9.59	9.34	9.65	11.83	9.55	10.49	10.49	10.57	10.51	12.10	10.44	9.70	9.65	10.46	11.82	10.54	10.55
Al	6.33	5.67	5.68	4.17	6.37	6.61	6.32	4.10	6.40	5.50	5.49	5.42	5.40	3.92	5.49	6.33	6.35	5.53	4.16	5.51	5.50
Ti	0	0	0	0	0	0	0	0	0	0	0	0	0	0	0.02	0	0	0	0	0	0
Fe_{+2}	0	0	0	0.03	0	0.01	0.03	0.04	0	0.01	0.02	0.01	0	0.03	0.03	0	0	0	0.03	0	0
Mn	0	0	0	0.01	0	0	0	0.01	0	0	0	0	0	0	0	0	0	0	0.01	0	0
Mg	0	0	0	0.01	0	0	0	0.05	0	0	0	0	0.01	0.02	0	0.01	0	0	0	0	0
Ca	2.29	1.59	1.63	0.31	2.41	2.69	2.33	0.29	2.50	1.48	1.45	1.41	1.63	0.18	1.55	2.22	2.32	1.54	0.29	1.40	1.43
Na	1.68	2.25	2.22	3.43	1.65	1.39	1.66	3.58	1.55	2.45	2.51	2.52	2.43	3.36	2.43	1.69	1.64	2.45	3.53	2.45	2.39
K	0.05	0.05	0.03	0.02	0.03	0.01	0.03	0.02	0.03	0.09	0.10	0.10	0.05	0.01	0.08	0.03	0.04	0.05	0.02	0.07	0.03
End members (%)																					
Ab	41.8	57.9	57.2	91.4	40.4	34	41.3	92.1	37.9	61	61.8	62.6	59.1	94.8	60	42.9	40.9	60.6	91.9	62.5	62.1
An	57	40.7	42	8.2	59	65.7	58.1	7.4	61.4	36.8	35.7	35	39.7	5.1	38.2	56.4	58.1	38.1	7.6	35.8	37.1
Or	1.2	1.4	0.7	0.4	0.7	0.3	0.6	0.5	0.7	2.3	2.4	2.4	1.2	0.2	1.9	0.7	1	1.3	0.5	1.7	0.8

Rock type	Quartz-diorite																							
Sample No.	Sh31																							
Mineral	K-feldspar					Plagioclase														Zoned plagioclase				
Spot No.	Kf-6	Kf-20	Kf-34	Kf-48	Kf-63	Pl-3	Pl-9	Pl-13	Pl-26	Pl-29	Pl-40	Pl-44	Pl-46	Pl-51	Pl-54	Pl-58	Pl-68	Pl-74	Pl-76	Pl-78	$Pl\text{-}5^C$	$Pl\text{-}15^C$	$Pl\text{-}40^C$	Pl-6R	$Pl\text{-}16^R$	$Pl\text{-}41^R$
Major oxides (wt.%)																										
SiO_2	64.20	64.05	64.81	64.09	64.07	61.60	61.56	58.57	59.28	58.57	59.29	58.45	60.68	61.56	58.81	56.81	60.59	60.86	59.43	58.74	53.24	52.88	53.29	59.41	59.49	60.75
TiO_2	0.01	0.00	0.00	0.05	0.01	0.00	0.00	0.05	0.03	0.01	0.00	0.00	0.00	0.04	0.05	0.00	0.07	0.00	0.08	0.00	0.00	0.00	0.00	0.03	0.00	0.03
Al_2O_3	18.46	18.37	18.48	18.63	18.68	23.72	23.99	25.61	25.34	25.75	25.15	25.57	23.53	23.96	25.66	27.55	24.10	24.47	25.40	25.34	29.66	29.62	29.23	25.24	25.62	24.08
FeO	0.21	0.17	0.10	0.14	0.13	0.09	0.07	0.22	0.18	0.12	0.23	0.08	0.00	0.22	0.22	0.07	0.26	0.06	0.09	0.11	0.16	0.03	0.00	0.08	0.12	0.14
MnO	0.01	0.00	0.01	0.01	0.00	0.01	0.01	0.01	0.02	0.00	0.02	0.00	0.00	0.00	0.00	0.00	0.03	0.01	0.00	0.00	0.00	0.00	0.00	0.00	0.01	0.00
MgO	0.00	0.00	0.00	0.00	0.00	0.00	0.00	0.00	0.00	0.00	0.00	0.00	0.00	0.00	0.00	0.00	0.00	0.00	0.00	0.00	0.00	0.01	0.00	0.00	0.00	0.00
CaO	0.00	0.00	0.00	0.02	0.00	4.95	4.66	7.26	6.93	7.23	6.76	7.51	4.67	5.28	7.26	9.14	5.60	5.59	6.87	6.93	11.87	12.26	11.81	6.55	6.82	5.63
Na_2O	0.21	0.31	0.70	0.52	0.56	8.56	8.69	7.25	7.23	7.28	7.37	7.28	7.48	8.44	7.24	6.32	8.16	8.29	7.41	7.51	4.69	4.57	4.67	7.56	7.45	8.29
K_2O	16.11	16.05	15.39	15.30	16.47	0.28	0.42	0.36	0.54	0.29	0.59	0.38	2.73	0.27	0.42	0.18	0.38	0.22	0.25	0.38	0.14	0.10	0.06	1.05	0.36	0.21
Total	99.20	98.95	99.50	98.76	99.93	99.20	99.40	99.32	99.54	99.24	99.42	99.26	99.09	99.78	99.66	100.08	99.20	99.50	99.28	99.02	99.76	99.47	99.15	99.93	99.93	99.13
Structural formulae																										
Si	11.96	11.97	12	11.95	11.9	11.01	10.99	10.55	10.64	10.54	10.66	10.54	10.97	10.96	10.55	10.2	10.87	10.87	10.64	10.6	9.658	9.626	9.718	10.65	10.63	10.89
Al	4.051	4.042	4.028	4.092	4.084	4.993	5.042	5.431	5.355	5.458	5.323	5.428	5.011	5.023	5.422	5.82	5.094	5.145	5.357	5.385	6.335	6.348	6.277	5.325	5.389	5.086
Ti	0.002	0	0	0.006	0.002	0	0	0.007	0.003	0.001	0	0	0	0.006	0.007	0	0.009	0	0.011	0	0	0	0	0.005	0	0.004
Fe_{+2}	0.032	0.026	0.016	0.021	0.021	0.013	0.01	0.033	0.027	0.018	0.035	0.011	0	0.032	0.033	0.01	0.039	0.009	0.013	0.017	0.025	0.005	0	0.013	0.017	0.021
Mn	0.001	0	0.001	0.002	0	0.001	0.002	0.002	0.003	0	0.003	0	0	0	0	0	0.005	0.001	0	0	0	0	0	0	0.002	0
Mg	0	0	0.001	0	0.001	0	0	0	0	0	0.001	0	0	0	0	0	0	0	0	0	0	0.002	0	0	0	0
Ca	0	0	0	0.004	0	0.949	0.891	1.4	1.332	1.394	1.302	1.45	0.906	1.007	1.396	1.76	1.077	1.069	1.319	1.341	2.307	2.391	2.307	1.257	1.305	1.082
Na	0.075	0.11	0.253	0.186	0.202	2.966	3.007	2.53	2.514	2.541	2.57	2.543	2.623	2.914	2.52	2.2	2.838	2.871	2.574	2.629	1.648	1.614	1.651	2.627	2.579	2.882
K	3.83	3.83	3.63	3.64	3.90	0.06	0.10	0.08	0.12	0.07	0.13	0.09	0.63	0.06	0.10	0.04	0.09	0.05	0.06	0.09	0.03	0.02	0.01	0.24	0.08	0.05
End members (%)																										
Ab	1.9	2.8	6.5	4.9	4.9	74.5	75.3	63.1	63.3	63.5	64.2	62.3	63.1	73.2	62.8	55	70.9	71.9	65.2	64.8	41.3	40.1	41.6	63.7	65	71.8
An	0	0	0	0.1	0	23.9	22.3	34.9	33.6	34.8	32.5	35.5	21.8	25.3	34.8	44	26.9	26.8	33.4	33.1	57.8	59.4	58.1	30.5	32.9	27
Or	98.1	97.2	93.5	95	95.1	1.6	2.4	2	3.1	1.6	3.3	2.2	15.1	1.5	2.4	1.1	2.2	1.3	1.4	2.1	0.8	0.5	0.4	5.8	2.1	1.2

C = core, R=rim

TABLE VI. Electron microprobe analyses of the Fe-Ti oxides in the Shahira layered mafic intrusion

Rock type	Chilled margin							Hornblende gabbro								Quartz-diorite					
Mineral	Magnetite																				
Sample No.	Sh3							Sh20								Sh31					
Spot No.	mt#11	mt#28	mt#33	mt#41	mt#49	mt#52	mt#64	mt#16	mt#24	mt#33	mt#37	mt#45	mt#49	mt#56	mt#71	mt#8	mt#25	mt#31	mt#41	mt#54	mt#68
Major oxides (wt. %)																					
SiO_2	0,06	0,08	0,01	0,08	0,05	0,00	0,00	0,00	0,03	0,04	0,03	0,03	0,00	0,00	0,00	0,00	0,00	0,00	0,05	0,02	0,00
TiO_2	0,55	0,23	0,07	0,31	0,17	0,14	0,14	0,55	0,27	0,20	0,26	0,18	0,14	0,26	0,17	0,25	0,32	0,14	0,27	0,63	0,27
Al_2O_3	0,22	0,25	0,07	0,04	0,06	0,08	0,08	0,00	0,38	0,20	0,18	0,13	0,06	0,08	0,00	0,00	0,04	0,04	0,26	0,17	0,01
$FeO_{(T)}$	90,16	92,25	90,28	89,28	89,57	87,74	89,35	89,29	90,15	89,55	92,22	92,43	87,76	90,89	91,71	91,61	89,34	88,52	90,69	91,61	92,18
MnO	0,04	0,05	0,01	0,19	0,20	0,17	0,16	0,08	0,01	0,04	0,07	0,04	0,14	0,16	0,19	0,19	0,17	0,20	0,01	0,09	0,21
MgO	0,01	0,02	0,01	0,00	0,00	0,00	0,00	0,00	0,01	0,01	0,00	0,01	0,00	0,00	0,00	0,01	0,00	0,00	0,02	0,00	0,00
CaO	0,04	0,01	0,01	0,04	0,04	0,04	0,02	0,08	0,02	0,01	0,01	0,03	0,02	0,25	0,16	0,10	0,03	0,04	0,03	0,00	0,07
Na_2O	0,03	0,04	0,01	0,00	0,00	0,01	0,00	0,00	0,01	0,03	0,03	0,01	0,00	0,01	0,01	0,00	0,01	0,00	0,03	0,02	0,00
K_2O	0,00	0,01	0,00	0,02	0,04	0,06	0,06	0,02	0,00	0,01	0,01	0,01	0,07	0,05	0,06	0,05	0,07	0,06	0,00	0,01	0,07
Cr_2O_3	0,22	0,24	0,44	0,49	0,37	0,19	0,13	0,09	0,07	0,07	0,09	0,11	0,11	0,03	0,12	0,06	0,05	0,06	0,00	0,03	0,09
Total	91,35	93,16	90,91	90,44	90,49	88,42	89,94	90,10	90,94	90,16	92,90	93,00	88,29	91,74	92,41	92,27	90,02	89,06	91,36	92,58	92,89
Structural formulae																					
Si	0	0	0	0	0	0	0	0	0	0	0	0	0	0	0	0	0	0	0	0	0
Ti	0,02	0,01	0	0,01	0	0	0	0,02	0,01	0,01	0,01	0,01	0	0,01	0	0,01	0,01	0	0,01	0,02	0,01
Al	0,01	0,01	0	0	0	0	0	0	0,02	0,01	0,01	0,01	0	0	0	0	0	0	0,01	0,01	0
Fe^{+3}	1,94	1,96	1,98	1,96	1,97	1,98	1,98	1,96	1,96	1,97	1,97	1,98	1,98	1,98	1,99	1,98	1,98	1,99	1,97	1,95	1,98
Fe^{+2}	1,01	1,01	1	1	1	1	1	1,01	1,01	1	1,01	1	1	0,99	0,99	1	1	1	1,01	1,02	1
Mn	0	0	0	0,01	0,01	0,01	0,01	0	0	0	0	0	0	0,01	0,01	0,01	0,01	0,01	0	0	0,01
Mg	0	0	0	0	0	0	0	0	0	0	0	0	0	0	0	0	0	0	0	0	0
Ca	0	0	0	0	0	0	0	0	0	0	0	0	0	0,01	0,01	0	0	0	0	0	0
Na	0	0	0	0	0	0	0	0	0	0	0	0	0	0	0	0	0	0	0	0	0
K	0	0	0	0	0	0	0	0	0	0	0	0	0	0	0	0	0	0	0	0	0
Cr	0,01	0,01	0,01	0,02	0,01	0,01	0	0	0	0	0	0	0	0	0	0	0	0	0	0	0
Xulv	0,02	0,01	0	0,01	0	0	0	0,02	0,01	0,01	0,01	0,01	0	0,01	0	0,01	0,01	0	0,01	0,02	0,01

Rock type	Chilled margin				Hornblende gabbro					Quartz-diorite					
Mineral	Ilmenite														
Sample No.	Ch3				Ch20					Ch31					
Spot No.	ilm10	ilm31	ilm88	ilm89	ilm15	ilm32	ilm57	ilm60	ilm84	ilm20	ilm27	ilm41	ilm53	ilm69	ilm70
Major oxides (wt. %)															
SiO_2	0.00	0.00	0.00	0.00	0.03	0.00	0.00	0.00	0.02	0.04	0.03	0.03	0.04	0.02	0.03
TiO_2	52.03	51.36	52.06	52.47	47.52	49.80	50.06	50.63	49.95	48.21	49.00	46.24	47.87	47.33	47.34
Al_2O_3	0.01	0.00	0.00	0.00	0.00	0.00	0.00	0.00	0.01	0.01	0.02	0.00	0.02	0.00	0.01
FeO(T)	43.31	44.10	43.08	43.04	45.34	42.92	43.62	43.82	45.13	44.47	45.63	48.60	46.57	47.56	48.17
MnO	0.99	1.02	0.83	0.72	1.24	1.65	0.80	0.79	1.12	2.48	2.07	1.65	2.05	2.13	2.20
MgO	0.07	0.15	0.00	0.07	0.08	0.05	0.00	0.00	0.05	0.15	0.09	0.10	0.16	0.17	0.17
CaO	0.04	0.00	0.10	0.01	0.03	0.02	0.20	0.10	0.12	0.00	0.07	0.01	0.02	0.02	0.02
Na_2O	0.00	0.01	0.01	0.00	0.01	0.00	0.00	0.01	0.01	0.00	0.02	0.00	0.03	0.00	0.02
K_2O	0.00	0.00	0.01	0.01	0.00	0.01	0.01	0.01	0.01	0.00	0.01	0.00	0.00	0.01	0.00
Cr_2O_3	0.18	0.21	0.17	0.09	0.17	0.20	0.30	0.17	0.21	0.21	0.21	0.09	0.16	0.08	0.10
Total	96.62	96.85	96.26	96.40	94.41	94.64	94.99	95.53	96.63	95.56	97.15	96.73	96.90	97.31	98.06
Structural formulae															
Si	0	0	0	0	0	0	0	0	0	0	0	0	0	0	0
Ti	1.02	1.01	1.03	1.04	0.95	1	1	1.01	0.98	0.95	0.95	0.90	0.93	0.92	0.91
Al	0	0	0	0	0	0	0	0	0	0	0	0	0	0	0
Fe^{+3}	-0.05	-0.02	-0.06	-0.07	0.09	0	-0.01	-0.02	0.03	0.08	0.08	0.19	0.13	0.16	0.17
Fe^{+2}	1	0.98	1.01	1.02	0.92	0.96	0.98	0.99	0.95	0.89	0.90	0.86	0.88	0.87	0.86
Mn	0.02	0.02	0.02	0.02	0.03	0.04	0.02	0.02	0.02	0.06	0.05	0.04	0.04	0.05	0.05
Mg	0	0.01	0	0	0	0	0	0	0	0.01	0	0	0.01	0.01	0.01
Ca	0	0	0	0	0	0	0.01	0	0	0	0	0	0	0	0
Na	0	0	0	0	0	0	0	0	0	0	0	0	0	0	0
K	0	0	0	0	0	0	0	0	0	0	0	0	0	0	0
Cr	0	0	0	0	0	0	0.01	0	0	0	0	0	0	0	0
Xilm	1.03	1.01	1.03	1.04	0.95	1	1	1.01	0.98	0.96	0.96	0.90	0.93	0.92	0.91